NASA Technical Paper 2800

1988

Static Performance of an Axisymmetric Nozzle With Post-Exit Vanes for Multiaxis Thrust Vectoring

Bobby L. Berrier
and Mary L. Mason

Langley Research Center
Hampton, Virginia

NASA
National Aeronautics
and Space Administration

Scientific and Technical Information Division

Summary

An investigation was conducted in the static test facility of the Langley 16-Foot Transonic Tunnel to determine the flow-turning capability and the nozzle internal performance of an axisymmetric convergent-divergent nozzle with post-exit vanes installed for multiaxis thrust vectoring. The effects of vane curvature, vane location relative to the nozzle exit, number of vanes, and vane deflection angle were determined. A comparison of the post-exit-vane thrust-vectoring concept with other thrust-vectoring concepts is provided. All tests were conducted with no external flow, and nozzle pressure ratio was varied from 1.6 to 6.0.

Results of this study indicate that the thrust-vectoring capability of some of the present post-exit-vane configurations was competitive with other thrust-vectoring concepts reported in the literature. However, all the present post-exit-vane configurations incurred large resultant gross-thrust losses to achieve vectored thrust. In general, any change in geometry which produced larger thrust-vector angles also caused larger resultant thrust losses.

Introduction

Future fighter aircraft must possess improved performance over a broader range of flight conditions than any aircraft previously developed. Much of this improved performance will be directly related to propulsion system advances. Using the exhaust nozzle to direct the thrust force vector (thrust vectoring) away from the usual axial direction has the potential of providing substantial airplane performance gains or even adding new capabilities (refs. 1 to 9). Early thrust-vectoring studies were limited to the longitudinal or pitch axis (refs. 1, 6, and 10 to 14).

Recent studies have shown that multiaxis thrust vectoring (pitch and yaw axes) can provide additional benefits beyond those obtained from pure pitch thrust vectoring. The major benefit of multiaxis thrust vectoring is aircraft control augmentation (refs. 8 and 15 to 24). Use of the thrust force vector for aircraft control will allow aircraft designers to reduce or even eliminate conventional aerodynamic control surfaces and should lead to aircraft designs with lower weight and drag and improved survivability resulting from visual and radar cross-section reductions (ref. 23). Also, use of thrust vectoring for control will allow aircraft to operate in flight regimes where conventional aerodynamic controls are ineffective, namely, at very low speeds and at very high angles of attack. Maneuvers in these flight regimes have been termed post-stall maneuvers or "supermaneuverability" (refs. 15, 19, and 22 to 24).

Few experimental investigations of nozzles which can provide yaw thrust vectoring or simultaneous pitch and yaw thrust vectoring have been reported (refs. 25 to 27). The purpose of the present paper is to present the results of an investigation to evaluate the effectiveness of post-exit vanes in providing a pitch and yaw capability, singularly or simultaneously, for an axisymmetric convergent-divergent nozzle. The experimental investigation was conducted in the static test facility of the Langley 16-Foot Transonic Tunnel at static (no external flow) conditions. The model geometric parameters investigated were number of vanes, vane curvature, vane location relative to the nozzle exit, and vane deflection angle. Nozzle internal performance and the flow-turning capability of the various vane configurations are presented for nozzle pressure ratios from 1.6 to 6.0. High-pressure air was used to simulate the jet exhaust flow.

Symbols

All forces (with the exception of resultant gross thrust) and angles are referred to the model centerline (body axis).

A_e	nozzle exit area, in^2
A_t	nozzle throat area, in^2
C_d	nozzle discharge coefficient, w_p/w_i
c_v	chord length of vane, in.
F	measured thrust along body axis, positive in forward direction, lbf
F_i	ideal gross thrust, $w_p\sqrt{\frac{R_j T_{t,j}}{g}\frac{2\gamma}{\gamma-1}\left[1-\left(\frac{p_a}{p_{t,j}}\right)^{(\gamma-1)/\gamma}\right]}$, lbf
F_N	measured normal force, positive up, lbf
F_r	resultant gross thrust, $\sqrt{F^2+F_N^2+F_S^2}$, lbf
F_S	measured side force, positive to right, lbf
g	acceleration due to gravity, 32.174 ft/sec^2
N	number of vane positions on configuration (either 3 or 4)
NPR	nozzle pressure ratio, $p_{t,j}/p_a$
$(NPR)_{des}$	design nozzle pressure ratio (NPR for fully expanded flow at nozzle exit)
p_a	ambient pressure, psi

$p_{t,j}$	jet total pressure, psi
R	radius of nozzle exit, in.
R_j	jet gas constant, 53.36 ft/°R
R_v	vane radius of curvature (see fig. 3(b)), in.
r_h	radius from model centerline to leading edge of vane, in.
$T_{t,j}$	jet total temperature, °R
w_i	ideal weight-flow rate, lbf/sec
w_p	measured weight-flow rate, lbf/sec
x_h	axial distance from nozzle exit plane to leading edge of vane, positive downstream, in.
x_v	axial distance downstream of vane leading edge (see fig. 3(b)), in.
γ	ratio of specific heats, 1.3997 for air
Δ	increment between unvectored and vectored parameter
δ_{est}	estimated vector angle, deg
δ_p	resultant pitch-vector angle, $\tan^{-1}\frac{F_N}{F}$, deg
δ_r	resultant vector angle, $\sqrt{\delta_p^2 + \delta_y^2}$, deg
δ_s	resultant splay vector angle, positive in clockwise direction from nozzle top, $\tan^{-1}\frac{F_S}{F_N}$, deg
δ_v	geometric vane angle, deg
$\delta_{v,p}$	geometric pitch-vector angle measured from model centerline, positive angle produces positive normal-force output, deg
$\delta_{v,y}$	geometric yaw-vector angle measured from model centerline, positive angle produces positive side-force output, deg
$\delta_{v,V1}, \ldots, \delta_{v,V4}$	geometric vane deflection angles for each individual vane, positive for trailing-edge deflection toward nozzle centerline (see fig. 4(a)), deg
δ_y	resultant yaw-vector angle, $\tan^{-1}\frac{F_S}{F}$, deg
$\eta_{r_{\delta_p}}$	resultant gross-thrust efficiency parameter with pitch thrust vectoring (eq. (6)), per deg
$\eta_{r_{\delta_r}}$	resultant gross-thrust efficiency parameter with simultaneous pitch and yaw thrust vectoring (eq. (9)), per deg
$\eta_{r_{\delta_y}}$	resultant gross-thrust efficiency parameter with yaw thrust vectoring (eq. (8)), per deg
η_{δ_p}	body-axis-thrust efficiency parameter with pitch thrust vectoring (eq. (5)), per deg
η_{δ_y}	body-axis-thrust efficiency parameter with yaw thrust vectoring (eq. (7)), per deg
ϕ	meridian angle of vane centerline about model roll axis, positive clockwise looking upstream (see fig. 4(a)), deg

Abbreviations:

Axi.	axisymmetric
C-D	convergent-divergent
Conf.	configuration
conv.	convergent
DC	double curvature
div.	divergent
R	radius
SC	single curvature
SERN	single expansion ramp nozzle
Sta.	model station, in.
typ.	typical
V1, V2, V3, V4	vane 1, vane 2, etc. (see fig. 4(a))
2-D	two-dimensional

Apparatus and Methods

Static Test Facility

This investigation was conducted in the static test facility of the Langley 16-Foot Transonic Tunnel. Testing is conducted in a large room where the jet from a simulated single-engine propulsion system exhausts to the atmosphere through a large open doorway. A control room is remotely located from the test

area, and a closed-circuit television is used to observe the model when the jet is operating. The static test facility has an air control system which is similar to that of the 16-Foot Transonic Tunnel and includes valving, filters, and a heat exchanger to maintain the jet flow at constant stagnation temperature. The air system utilizes the same clean, dry air supply as that used by the 16-Foot Transonic Tunnel (ref. 28).

Single-Engine Propulsion Simulation System

A sketch of the single-engine air-powered nacelle model on which various thrust-vectoring nozzle configurations were tested is presented in figure 1. The propulsion simulation system is shown with a typical post-exit-vane configuration installed.

An external high-pressure air system provided a continuous flow of clean, dry air at a controlled temperature of about 540°R. This high-pressure air was varied during jet simulation up to about 90 psi in the nozzle. The pressurized air was brought by six air lines through a dolly-mounted support strut and into a high-pressure plenum chamber. The air was then discharged perpendicularly into the model low-pressure plenum through eight multiholed sonic nozzles equally spaced around the high-pressure plenum. (See fig. 1.) This airflow system was designed to minimize any forces imposed by the transfer of axial momentum as the air is passed from the nonmetric high-pressure plenum to the metric (attached to the balance) low-pressure plenum. Two flexible metal bellows seal the air system (between metric and nonmetric model parts) and compensate for axial forces caused by pressurization. The air then passed from the low-pressure plenum through a circular choke plate and instrumentation section, which were common for all nozzle configurations tested. All test configurations attached to the instrumentation section at model station 39.00.

Nozzle and Post-Exit-Vane Design

Nozzle. The nozzle utilized throughout this investigation was an axisymmetric, convergent-divergent type. Figure 2 is a sketch showing the geometry of the nozzle. The nozzle had a throat area A_t of 3.145 in^2, an expansion ratio A_e/A_t of 1.482, and a design nozzle pressure ratio $(NPR)_{des}$ (NPR for fully expanded flow at nozzle exit) of 6.09.

Post-exit vanes. The thrust-vectoring concept investigated consisted of vanes mounted downstream of the nozzle exit (post-exit vanes). Figure 3 presents sketches showing the geometry of the vanes. The vane planform was not varied during the investigation except for clipping the trailing-edge corners (see fig. 3(a)) for the configurations utilizing four post-exit vanes. This modification was required to prevent physical interference between vanes at large positive deflections. Two vane curvature geometries were tested (fig. 3(b)). A double-curvature ("spoon" shaped) vane, set with axial and radial curvature, and a single-curvature vane, set with radial curvature only, were tested.

As shown in figure 1, the post-exit vanes were mounted externally on the axisymmetric C-D nozzle. For ease of configuration changes, the vanes were attached by two bolts to a mounting bar through a machined slot (see fig. 3(a)) in the vane mounting plate, which made vane deflections possible at any angle between −25° and 25°.

Two basic thrust-vectoring concepts were investigated, namely, a three-vane concept and a four-vane concept. Figure 4 presents sketches showing the circumferential, longitudinal, and radial locations of the vanes relative to the nozzle exit. The three-vane concept had three post-exit vanes mounted equiangularly (120° apart) around the nozzle exit. Figure 5 presents photographs of several of these configurations. The four-vane concept had four post-exit vanes mounted equiangularly (90° apart) around the nozzle exit (see fig. 4). Photographs of several four-vane configurations are shown in figure 6. Examination of figure 4(a) indicates that obtaining a pure pitch thrust vector is straightforward on both thrust-vectoring concepts (deflection of vanes V1 and V3 for the four-vane configurations and deflection of vane V1 or vanes V2 and V3 for the three-vane configurations). Similarly, obtaining a pure yaw thrust vector is straightforward for the four-vane configurations (deflection of vanes V2 and V4). However, obtaining a pure yaw thrust vector for the three-vane configurations is not obvious and probably requires unequal deflections of two or possibly all three vanes.

The effect of vane longitudinal and radial position relative to the nozzle exit was investigated for a single vane at $\phi = 240°$. Sketches showing the longitudinal and radial variations from the baseline position are given in figure 4(b). These configurations represent a three-vane configuration with vanes V1 and V3 removed. All other configurations investigated had vanes located in the baseline position only.

Instrumentation

A six-component strain-gauge balance was used to measure the forces and moments on the model downstream of model station 20.50. Jet total pressure was measured at a fixed station in the instrumentation section by a five-probe rake. (See fig. 1.) A thermocouple was also positioned in

the instrumentation section to measure the jet total temperature. Weight flow of the high-pressure air supplied to the nozzle was determined from pressure and temperature measurements in the high-pressure plenum calibrated with Stratford choke nozzles (ref. 29).

Data Reduction

Approximately 50 frames of data, taken at a rate of 10 frames per second, were used for each data point; average values were used in the computations. With the exception of resultant gross thrust F_r, all data in this report are referenced to the model centerline. Six basic performance parameters are used in the presentation of results; they are internal thrust ratio F/F_i, resultant gross-thrust ratio F_r/F_i, discharge coefficient C_d, and three resultant thrust-vector angles—pitch δ_p, yaw δ_y, and splay δ_s. Reference 30 presents a detailed description of the data reduction procedures used for the current investigation.

Internal thrust ratio F/F_i is the ratio of the actual measured nozzle thrust along the body axis to the ideal nozzle thrust. Ideal thrust F_i is based on measured weight flow w_p, jet total pressure $p_{t,j}$, and jet total temperature $T_{t,j}$. (See the section "Symbols.") The balance axial-force measurement, from which the actual nozzle thrust F is subsequently obtained, is initially corrected for model weight tares and balance interactions. Although the bellows arrangement in the air pressurization system was designed to eliminate pressure and momentum interactions with the balance, small bellows tares on the six balance components still exist. These tares result from a small pressure difference between the ends of the bellows when air system internal velocities are high and from small differences in the forward and aft bellows spring constants when the bellows are pressurized. These bellows tares were determined by running Stratford choke calibration nozzles with known performance over a range of expected internal pressures and external forces and moments. The resulting tares were then applied to the six-component balance data obtained during the current investigation. Balance axial force obtained in this manner is a direct measurement of the thrust along the body axis F. The procedure for computing the bellows tares is discussed in detail in reference 28.

The resultant thrust ratio F_r/F_i is the resultant gross thrust divided by the ideal thrust. Resultant gross thrust is obtained from the measured axial, normal, and side components of the jet resultant force. From the definitions of F and F_r, it is obvious that the thrust along the body axis F includes losses which result from turning the exhaust vector away from the axial direction, whereas resultant gross thrust F_r does not.

Nozzle discharge coefficient C_d is the ratio of measured weight flow to ideal weight flow where ideal weight flow (in lbf/sec) is computed from equation (1) or (2), depending on the value of NPR. If NPR $\leq$ 1.89 (unchoked nozzle flow)

$$w_i = A_t p_{t,j} \left(\frac{1}{\mathrm{NPR}}\right)^{1/\gamma} \sqrt{\frac{2g}{T_{t,j} R_j} \frac{\gamma}{(\gamma-1)} \left[1 - \left(\frac{1}{\mathrm{NPR}}\right)^{(\gamma-1)/\gamma}\right]} \tag{1}$$

If NPR > 1.89 (choked nozzle flow)

$$w_i = A_t p_{t,j} \left(\frac{2}{\gamma+1}\right)^{(\gamma+1)/2(\gamma-1)} \sqrt{\frac{\gamma g}{T_{t,j} R_j}} \tag{2}$$

Nozzle discharge coefficient reflects the ability of a nozzle to pass weight flow and is reduced by any momentum and vena contracta losses (effective throat area less than A_t). Nozzle throat area A_t is the measured minimum area in the nozzle.

The resultant vector angles δ_p, δ_y, and δ_s are the angles at which the post-exit vanes turn the exhaust flow from the axial direction. As indicated in the "Symbols" section, determination of these angles requires the measurement of axial, normal, and side forces on the model. As an aid to data analysis, estimated vector angle δ_{est} (function of model geometry only) is shown on several of the summary plots. Estimated vector angle was obtained using equations (3) and (4). It is assumed in these equations that the effectiveness of each post-exit vane was inversely proportional to the number of vane locations on the configuration (e.g., each vane on a three-vane configuration affected only 1/3 of the exhaust flow). For estimated pitch-vector angles,

$$\delta_{\mathrm{est}} = \sum_{n=1}^{N} \frac{1}{N} \tan^{-1}\left[\frac{\sin(\delta_{v,n})\cos(\phi_n)}{\cos(\delta_{v,n})}\right] \tag{3}$$

For estimated yaw-vector angles,

$$\delta_{\mathrm{est}} = \sum_{n=1}^{N} \frac{1}{N} \tan^{-1}\left[\frac{\sin(\delta_{v,n})\sin(\phi_n)}{\cos(\delta_{v,n})}\right] \tag{4}$$

Also, several summary figures show estimates for configurations which were not tested. These estimates were based on data from actual tested configurations. On the four-vane configurations, for example, yaw thrust-vector angles caused by deflecting

vanes V2 and V4 (tested) should be identical to pitch thrust-vector angles caused by deflecting vanes V1 and V3 (not tested), except that forces and angles are rolled by 90°.

To compare results from the current investigation with results obtained from previous investigations, several new thrust efficiency parameters were defined. For pure pitch thrust-vectoring concepts (no yaw), a body-axis-thrust efficiency parameter is defined as

$$\eta_{\delta_p} = \frac{\Delta(F/F_i)}{|\delta_p|} \tag{5}$$

and a resultant gross-thrust efficiency parameter is defined as

$$\eta_{r_{\delta_p}} = \frac{\Delta(F_r/F_i)}{|\delta_p|} \tag{6}$$

For pure yaw thrust-vectoring concepts (no pitch), the body-axis-thrust efficiency parameter is defined as

$$\eta_{\delta_y} = \frac{\Delta(F/F_i)}{|\delta_y|} \tag{7}$$

and the resultant gross-thrust efficiency parameter is defined as

$$\eta_{r_{\delta_y}} = \frac{\Delta(F_r/F_i)}{|\delta_y|} \tag{8}$$

For simultaneous pitch and yaw thrust-vectoring concepts, a resultant gross-thrust efficiency parameter is defined as

$$\eta_{r_{\delta_r}} = \frac{\Delta(F_r/F_i)}{\delta_r} \tag{9}$$

These parameters were computed from data obtained as close to $(\mathrm{NPR})_{\mathrm{des}}$ as possible and essentially indicate the amount of thrust loss resulting from 1° of resultant thrust-vector angle.

Results and Discussion

Basic Data

The basic data for each configuration of the current investigation are presented in figures 7 to 10. Data are presented in the form of resultant thrust ratio F_r/F_i, thrust ratio F/F_i, discharge coefficient C_d, resultant splay vector angle δ_s, resultant yaw-vector angle δ_y, and resultant pitch-vector angle δ_p. All basic data are plotted as functions of nozzle pressure ratio NPR. From the definitions of F and F_r, it is obvious that thrust ratio F/F_i includes losses which result from turning the exhaust vector away from the axial direction, whereas resultant thrust ratio F_r/F_i does not. Losses included in both thrust terms are friction and pressure drags associated with the thrust-vectoring hardware and any changes in geometry caused by the hardware.

In general, many of the basic data show trends consistent with previous studies (refs. 11, 13, 14, and 25 to 27). The vane-off nozzle configurations and many of the vane-on configurations have peak thrust performance (F and F_r) at a nozzle pressure ratio near the design value of 6.09. Nozzle overexpansion losses occur at NPR < 6.09 and, although not tested, it is expected that nozzle underexpansion losses would occur at NPR > 6.09. As expected, since all the geometric variables of the current test were well downstream of the nozzle throat, nozzle discharge coefficient was not affected by vane installation or deflection. Also, discharge coefficient was relatively independent of NPR once choked flow was established in the nozzle (NPR > 1.89). Positive deflection of a thrust-vector vane (vane trailing edge toward nozzle centerline) produced appropriate increases in the absolute values of resultant pitch and yaw-vector angles. As is discussed in more detail subsequently, negative deflections of the thrust-vector vane had little effect on δ_y and δ_p. The variation of resultant splay angle δ_s with vane deflection was also as expected. For example, for a single vane installed at $\phi = 240°$ (see fig. 7), vane deflection produced values of δ_s of about $-120°$ (equivalent to 240°). For the configuration with a vane installed at $\phi = 240°$ with a positive deflection of 25° and a vane installed at $\phi = 120°$ with varying deflection angles (see fig. 9(b)), resultant splay angle varied from about −120° (simultaneous pitch and yaw thrust vectoring) to −180° (pure pitch thrust vectoring) as vane deflection of the $\phi = 120°$ vane increased from negative to positive values.

The results discussed above were as expected based on previous investigations of convergent-divergent nozzles. However, the thrust parameters (F/F_i and F_r/F_i) exhibited two trends which were not easily anticipated from previous studies. First, the NPR at which peak thrust performance occurred tended to decrease with increasing positive vane deflection (vane deflecting into exhaust jet). This trend occurred even for the single-vane installation (see fig. 7), but it was most evident when multiple vanes were installed (see figs. 9(b) and 9(c)). Occurrence of peak thrust performance at lower values of NPR indicates that the design NPR has been reduced. Since $(\mathrm{NPR})_{\mathrm{des}}$ is proportional to nozzle expansion ratio A_e/A_t and throat area was not affected by vane deflection (as indicated by the independence of C_d to vane deflection), it is obvious that the nozzle effective exit area was reduced by positive vane deflections. This hypothesis is substantiated in figure 10(d). The data shown in figure 10(d) are for configurations with four vanes installed which deflect in unison. For these configurations, physical nozzle exit area must

decrease with increasing positive deflection angle, because all four vanes deflect simultaneously into the exhaust jet and, as can be noted from the thrust-ratio data, the NPR required for peak thrust performance subsequently decreases.

The second trend that was not expected is that many of the thrust performance curves (F/F_i and F_r/F_i) show either a discontinuity in curve slope or two distinct performance peaks. There are two possible causes for this behavior. At low NPR (NPR << $(NPR)_{des}$), internal exhaust flow separation probably occurs. As shown by the data in reference 31, internal flow separation can cause discontinuities in the thrust-ratio curves. Also, when vanes are installed or deflected unsymmetrically at the nozzle exit, part of the nozzle exhaust is bounded by an additional expansion surface, and the remainder of the exhaust flow is allowed to freely expand without any solid boundaries. In this case, the axisymmetric nozzle of the current test becomes similar to cone-plug, wedge, or single expansion ramp nozzles in that the exhaust is bounded on one side by a solid boundary and is allowed to freely expand on the other side. As shown in reference 13, nozzles of this type either have discontinuities in their thrust-ratio performance curves or have two distinct performance peaks.

Summary Data

Effect of vane curvature. A single vane mounted 120° counterclockwise from the nozzle top (the same position as vane V2 for the three-vane configurations) was used to investigate the effects of vane curvature. Basic data for the single-curvature and double-curvature vane configurations are presented in figures 7 and 9, respectively. Summary plots of the effects of vane curvature on thrust and resultant vector angles at NPR = 6.0 (near design) are presented in figure 11. For positive geometric-vane vector angles (vane deflected toward nozzle centerline), the single-curvature vane produced resultant thrust-vector angles (δ_y and δ_p) near the values expected (δ_{est}); the double-curvature vane produced resultant thrust-vector angles greater than δ_{est} (see fig. 11(a)). The double-curvature vane had better turning effectiveness, because the vane terminal angle was larger (by approximately 9.3°) than the geometric vane angle. Thus, the exhaust flow next to the double-curvature vane was turned to some value greater than $\delta_{v,V2}$. For negative geometric-vane vector angles, neither vane configuration produced any resultant thrust-vector angle. For NPR $\leq$ 6 (nozzle overexpanded or near design), the exhaust flow was probably not attached to either vane configuration at negative values of $\delta_{v,V2}$. It is possible that exhaust-flow attachment to the vane might occur for underexpanded nozzle operation (NPR > 6.09 for the test nozzle) as the jet plume starts to expand, but this condition was not tested during the current investigation.

As shown in figure 11(b), a positive deflection of the vane had a large detrimental effect on thrust performance. Losses in resultant thrust ratio of about 7 percent and 10 percent occurred at $\delta_{v,V2} = 25°$ for the single-curvature and double-curvature vanes, respectively. Resultant thrust ratio is not reduced by any loss in axial (body-axis) thrust as a result of turning the flow away from the axial direction. However, axial thrust ratio F/F_i includes this loss; thus, losses in axial thrust ratio are even greater than F_r/F_i losses. As indicated in reference 6, thrust vectoring a supersonic jet (as in the current investigation) tends to produce large resultant thrust losses. Such losses would occur only in the thrust-vectoring mode and are a function of the geometric post-exit-vane angle.

Negative post-exit-vane deflection caused only a very small loss in resultant thrust ratio for either vane curvature configuration. As previously discussed, such a result is consistent with the negligible effect of negative vane deflection angle on resultant thrust-vector angle. The small resultant thrust loss at negative vane deflections probably results from increased pressure drag as the vane axial projected area increases with increasing negative deflection. To reduce the model test matrix, only double-curvature vanes were used for the remainder of the test configurations.

Effect of vane location. The effect of post-exit-vane location relative to the nozzle exit (see fig. 4(b)) on body-axis-thrust efficiency with thrust vectoring is shown in figure 12. The body-axis-thrust efficiency parameters, η_{δ_p} and η_{δ_y}, indicate the amount of axial thrust ratio lost to provide 1° of resultant pitch or resultant yaw-vector angle, respectively. Efficient post-exit-vane thrust vectoring is represented by low values of the thrust efficiency parameter. For the data shown in figure 12, the single post-exit vane (position V2 on the three-vane configurations) was located 30° off the yaw axis and 60° off the pitch axis. Thus, this configuration was more efficient in producing resultant yaw-vector angles than resultant pitch-vector angles as indicated by lower values of η_{δ_y} than η_{δ_p}.

In general, moving the vane downstream from the baseline location (from $x_h/R = 0.089$ to $x_h/R = 0.310$) had only minor effects on vane turning efficiency. However, moving the vane radially away from the nozzle centerline (from $r_h/R = 1.190$ to

$r_h/R = 1.301$) produced significant reductions in vane turning efficiency (higher values of η_{δ_p} and η_{δ_y}) regardless of vane axial location. The loss in the body-axis-thrust efficiency parameters when the vane was moved away from the nozzle centerline was caused primarily by a decrease in resultant thrust-vector angle. For a given post-exit-vane deflection angle, the amount of vane area projecting into the exhaust stream decreases as the value of r_h/R increases. The baseline vane location was selected for tests on the remaining configurations.

Effect of vane deflection. The effects of vane deflection on the performance of three-vane and four-vane configurations (see fig. 4(a)) are presented in figures 13 and 14, respectively. The three-vane configuration (fig. 13) was tested with one, two, and three vanes installed. The four-vane configuration (fig. 14) was always tested with all four vanes installed, but with three different combinations of vane deflection angles. As discussed previously for the case of a single vane installed at $\phi = 240°$ (also shown in fig. 13), positive vane deflection generally produced an appropriate response in the resultant vector angles δ_p and δ_y (as indicated by the trends in δ_{est}) for all vane and configuration combinations tested. Unfortunately, positive vane deflections also produced large resultant and axial thrust-ratio losses, which increased with increasing geometric vane deflection angle and with the number of vanes which were set at a positive vane deflection. For the geometric variables of the current test, any change in geometry that produced larger resultant vector angles also produced larger thrust-ratio losses. As mentioned previously, these losses are probably associated with turning a supersonic jet (ref. 6).

Negative vane deflection generally had little effect on the thrust ratios or resultant vector angles. As discussed previously, the lack of jet flow attachment to the vanes at negative deflections (for the NPR of the current test) probably caused this result. One exception to this trend can be noted for the configuration shown in figure 14 with $\delta_{v,V1} = -25°$ and $\delta_{v,V2} = \delta_{v,V3} = 25°$. For this configuration, vanes V2 ($\phi = 270°$) and V3 ($\phi = 180°$) turn the exhaust flow toward vane V4 ($\phi = 90°$), and some exhaust-flow attachment on vane V4 probably occurs since negative deflection of vane V4 increases the magnitude of resultant yaw-vector angle (see fig. 14(c)).

The performance of the three-vane and four-vane configurations which produced the largest resultant vector angles at NPR = 6.0 is summarized in figures 15 and 16, respectively. For the three-vane configuration (fig. 15), the top vane was deflected outward ($\delta_{v,V1} = -25°$), the vane at $\phi = 240°$ was deflected inward ($\delta_{v,V2} = 25°$), and the deflection of the vane at $\phi = 120°$ was varied from $-25°$ to $25°$. For this configuration, maximum simultaneous pitch and yaw thrust vectoring is obtained when $\delta_{v,V3} = -25°$, and pure pitch thrust vectoring is obtained when $\delta_{v,V3} = 25°$. Examination of the data and sketch in figure 15 indicates two idiosyncrasies of a three-vane installation. First, it is impossible to generate pure yaw thrust vectoring with the configurations shown. Pure yaw thrust vectoring can only be obtained by setting a different vane deflection angle at each vane position. Second, a three-vane vectoring system produces different amounts of resultant pitch-vector angle in the negative and positive directions. Maximum negative resultant pitch-vector angle occurs when $\delta_{v,V1} = -25°$ and $\delta_{v,V2} = \delta_{v,V3} = 25°$ (two positive deflected vanes), but maximum positive resultant pitch-vector angle requires $\delta_{v,V1} = 25°$ and $\delta_{v,V2} = \delta_{v,V3} = -25°$ (only one positive deflected vane).

As shown in figure 15, increasing $\delta_{v,V3}$ from $-25°$ to $25°$ decreases the absolute value of resultant yaw-vector angle from about $10°$ to $0°$ and increases the absolute value of resultant pitch-vector angle from about $6°$ to $19°$. Resultant thrust-ratio losses associated with the three-vane post-exit-vane vectoring concept are very large. The resultant thrust-ratio loss increased from about 10 percent for one vane (V2) deflected toward the nozzle centerline to about 21 percent for two vanes (V2 and V3) deflected toward the nozzle centerline. Thrust losses of this magnitude are probably prohibitive for use on operational aircraft except for limited purposes. One potential application would be vane deflection only during take-off and landing mission segments. In this case, the thrust losses shown in figure 15 would not impact on the majority of the airplane mission, but the benefit of additional control during low dynamic pressure segments of flight could still be realized. Of course, any increase in weight because of the vectoring system would have to be considered for the entire mission. If control surfaces are sized for low dynamic pressure flight conditions, it is possible that the weight (and drag) of the vectoring system could be offset by resizing the control surfaces to a smaller size.

The effect of single-vane deflection on the performance of a nozzle with four post-exit vanes is shown in figure 16. Resultant thrust-ratio losses as a result of thrust vectoring for the four-vane configuration are larger than (because of the additional vane deflected toward the nozzle centerline), but similar in trends to, those shown in figure 15 for the three-vane configuration. Thus, thrust-ratio data are

not presented in figure 16. For the four-vane configuration shown, three vane deflections were held constant ($\delta_{v,V1} = -25°$ and $\delta_{v,V2} = \delta_{v,V3} = 25°$), and the fourth vane deflection ($\delta_{v,V4}$) was varied from −25° to 25°. For this configuration, maximum simultaneous pitch and yaw thrust vectoring is obtained when $\delta_{v,V4} = -25°$, and pure pitch thrust vectoring is obtained when $\delta_{v,V4} = 25°$. Unlike the three-vane configuration, pure pitch thrust vectoring or pure yaw thrust vectoring is easily obtained with the four-vane configuration. Also, the magnitudes of the resultant pitch- and yaw-vector angles are not dependent upon the direction of thrust vectoring. For $\delta_{v,V4} = -25°$, the absolute values of resultant pitch- and yaw-vector angles are both approximately 18°. As $\delta_{v,V4}$ increases (vane V4 deflects toward nozzle centerline), resultant pitch-vector angle δ_p remains reasonably constant (varies from −17° to −22°), but the absolute value of resultant yaw-vector angle δ_y decreases almost linearly to a value near 0° at $\delta_{v,V4} = 25°$. By visualizing the sketch of figure 16 rotated by 90°, it can be seen that identical results would be obtained for either pitch or yaw thrust vectoring.

Effect of number of vanes. The effect of number of post-exit vanes on the body-axis-thrust efficiency parameters is presented in figure 17. Low values of the thrust efficiency parameters indicate better (less loss) performance. The data presented in figure 17 indicate that performance depends not only on the number of vanes installed but also, as might be expected from previous discussion, on the number of vanes deflected toward the nozzle centerline. All the configurations shown in figure 17 exhibit very large thrust losses due to thrust vectoring. Body-axis-thrust ratio decreased by about 1 to 2 percent per degree of actual thrust-vector angle achieved.

One three-vane and two four-vane pitch-vectored configurations are shown in figure 17(a). However, each configuration has a different number of vanes deflected into the exhaust flow, and body-axis-thrust efficiency performance decreases (η_{δ_p} increases) with the number of positive deflected vanes. The data for the configuration with only one vane ($\phi = 180°$) deflected into the exhaust flow were estimated by rolling the thrust components of a yaw-vectored configuration by 90° about the body axis. A comparison of a three-vane and a four-vane configuration with the same number (one) of positive deflected vanes is shown in figure 17(b). The four-vane configuration has slightly better (lower η_{δ_y}) body-axis-thrust efficiency with yaw thrust vectoring than the three-vane configuration. This result might be expected since the four-vane configuration has a vane located perpendicular to the yaw axis (V2 at $\phi = 270°$); the three-vane configuration has its primary yaw vane (V2 at $\phi = 240°$) located 30° off the yaw axis. The three-vane configuration shown in figure 17(b) does not produce pure yaw; it also has a pitch component. A similar result is shown in figure 17(c) for the three-vane configuration. Since the vane used for simultaneous pitch and yaw vectoring (V2 at $\phi = 240°$) is located 60° off the pitch axis, the three-vane configuration exhibits very poor body-axis-thrust efficiency in the pitch direction (about 2 percent loss per degree of pitch-vector angle) when simultaneous pitch and yaw vectoring are required.

A comparison of the measured resultant thrust-vector angle envelopes for the three-vane and four-vane thrust-vector concepts (maximum vane deflection = ±25°) is presented in figure 18. The open symbols represent actual configurations tested, and the solid symbols represent envelope boundaries estimated from these data. For example, the upper left-hand boundary corner shown in figure 18 for the three-vane concept was estimated from data obtained on the pure negative pitch-vectored configuration (bottom of envelope) by rotating the measured resultant gross-thrust vector 120° clockwise and resolving normal- and side-force components. The upper boundary (positive pitch vectoring) was obtained in a similar manner from the data presented in figure 9(c) for the configuration with $\delta_{v,V2} = 25°$ and $\delta_{v,V1} = \delta_{v,V3} = -25°$.

The most obvious conclusion from the results shown in figure 18 is that the four-vane concept has a much larger resultant thrust-vector angle envelope than the three-vane concept, particularly for simultaneous yaw thrust vectoring and negative pitch thrust vectoring. Another result, which was discussed previously, is that the three-vane concept has an asymmetric vector angle envelope about the pitch axis.

Comparison of Thrust-Vectoring Concepts

The performances of pitch thrust-vectoring concepts, yaw thrust-vectoring concepts, and multiaxis thrust-vectoring concepts reported in references 26, 27, and 32 are compared with performance of the post-exit-vane vectoring concepts of the current investigation in figure 19. Data in this figure are presented at a nozzle pressure ratio near design for each concept shown. To eliminate the effect of different geometric vector angles tested for the various concepts, data on the vertical axes are presented in the form of a ratio, such that a value of 1.0 indicates a measured resultant vector angle equal to the geometric (metal) vector angle. The parameters on the horizontal axes indicate the loss in resultant (gross)

thrust ratio per degree of resultant vector angle obtained. A value of zero indicates no gross-thrust loss due to thrust vectoring.

Pitch thrust-vectoring concepts. Figure 19(a) shows that nozzles which use upper and lower internal flaps to provide pitch thrust vectoring (the 2-D C-D nozzles and one of the SERN concepts) can produce resultant pitch-vector angles near the geometric value ($\delta_p/\delta_{v,p} \approx 1.0$) with little or no gross-thrust loss ($\eta_{r_{\delta_p}} \approx 0$). A SERN with a flap in the trailing edge of the expansion ramp suffers from lower pitch thrust-vectoring effectiveness ($\delta_p/\delta_{v,p}$) and from larger thrust losses. Although the four-vane and three-vane (at positive pitch-vector angles) post-exit-vane concepts of the current investigation are competitive in pitch thrust-vectoring effectiveness with the other pitch-vectoring concepts shown, they incur substantially larger thrust losses. Because the post-exit-vane concept with three vanes utilizes only one vane to provide positive pitch thrust-vector angles, this configuration has the lowest pitch-vectoring effectiveness of any considered.

Yaw thrust-vectoring concepts. A comparison of the performance of several pure yaw-vectoring concepts is presented in figure 19(b). In general, except for the axisymmetric-nozzle post-exit-vane concept (four vanes) of the current investigation and a twin-engine configuration with dihedral 2-D C-D nozzles, the thrust-vectoring effectiveness of pure yaw thrust-vectoring concepts ($\delta_y/\delta_{v,y}$) is not as high as the thrust-vectoring effectiveness of the pure pitch thrust-vectoring concepts ($\delta_p/\delta_{v,p}$) shown in figure 19(a). The primary reason for the low yaw thrust-vectoring effectiveness of these configurations is the sizing of the yaw-vectoring mechanisms. Since 2-D nozzle aspect ratio is generally larger than 1.0, the yaw-vector flaps or vanes are either much smaller than the upper and lower pitch-vector flaps or they affect a smaller percentage of the total exhaust flow than the pitch-vector flaps. Also, as indicated in reference 26, the powered-rudder (center immersed vane) concept is penalized because the rudder chord is too short and the sidewall round-port concept is penalized because the port exhaust area is too small.

The 2-D C-D nozzle post-exit-vane, axisymmetric-nozzle post-exit-vane (current test), and powered-rudder concepts cause substantial resultant thrust losses because the yaw-vectoring mechanism is acting on a supersonic stream. However, the largest resultant thrust loss due to pure yaw vectoring was incurred by the sidewall round-port concept. For this concept, part of the exhaust flow is diverted out of the nozzle before reaching the primary nozzle throat and thus generates little or no resultant thrust.

The highest levels of pure yaw-vectoring effectiveness ($\delta_y/\delta_{v,y}$) were attained by the 2-D C-D, twin-engine dihedral nozzle concept of reference 27 and the axisymmetric-nozzle post-exit-vane (four vanes) concept of the current investigation. However, as previously discussed, the axisymmetric-nozzle post-exit-vane concept suffers from substantial resultant thrust loss in order to provide thrust-vector angles. It should be noted that pure yaw thrust vectoring was not obtained with the three-vane, axisymmetric-nozzle post-exit-vane concept. The 2-D C-D, dihedral nozzle concept is the only concept shown in figure 19 with high yaw-vectoring effectiveness and low resultant thrust loss. The reason for the low resultant thrust loss for this configuration is that it utilizes the same large upper and lower nozzle internal flaps used by the 2-D C-D nozzle concepts to generate high levels of pitch thrust-vectoring effectiveness with little or no resultant thrust loss (see fig. 19(a)). No additional flaps, vanes, or ports are required by this concept to generate yaw thrust vectoring.

Multiaxis thrust-vectoring concepts. The performance parameters presented in figure 19(c) are the same as those presented in figures 19(a) and 19(b) except for the resultant gross-thrust efficiency parameter ($\eta_{r_{\delta_r}}$), which is normalized by resultant vector angle. (See "Symbols" section.) Thus, a concept which is theoretically ideal in pitch thrust vectoring ($\delta_p/\delta_{v,p} = 1.0$; $\eta_{r_{\delta_p}} = 0$) is penalized by poor yaw thrust vectoring and vice versa. The concepts shown previously for pure pitch or yaw thrust vectoring generally exhibit similar performance trends when utilized for multiaxis (simultaneous pitch and yaw) thrust vectoring. Nozzles which utilize internal nozzle upper and lower flaps for pitch thrust vectoring exhibit good performance about the pitch thrust-vector axis; yaw-vectoring effectiveness is generally much lower than pitch-vectoring effectiveness; and the post-exit-vane concepts of the current investigation incur large resultant thrust-loss penalties.

The highest multiaxis thrust-vectoring performance is exhibited by a SERN with a tail-pipe gimbal joint. This configuration utilized both the nozzle expansion ramp and lower flap to obtain pitch thrust-vector angles. As discussed previously, this method provides high pitch thrust-vectoring effectiveness and little or no resultant thrust losses. Yaw thrust-vector angles were obtained by turning the flow upstream of the nozzle with a gimbal joint. Since exhaust-flow velocity ahead of the nozzle is very low, yaw-vector angles are obtained with no measurable loss

in thrust. This multiaxis thrust-vectoring concept appears to be ideally suited for a single-engine airplane application.

The twin-engine dihedral nozzle concept, which had good performance for both pure pitch and pure yaw thrust vectoring, shows a significant drop in both pitch and yaw thrust-vectoring effectiveness when used for multiaxis thrust vectoring. The reason for this performance decrease is that only one nozzle is deflected to obtain simultaneous pitch and yaw thrust vectors; thus, only half the available thrust is used to provide a multiaxis vector capability. The relatively high yaw-turning effectiveness and low resultant thrust loss of this concept, however, still make it attractive for twin-engine airplane applications where yaw tail-pipe gimbal joints may not be feasible. Also, since this concept requires no additional flaps, vanes, ports, actuators, etc., to obtain a multiaxis thrust-vectoring capability, it may have the lowest weight penalty of any of the concepts considered.

Conclusions

A static (no external flow) test has been conducted in the static test facility of the Langley 16-Foot Transonic Tunnel to determine the flow-turning capability and the nozzle internal performance of an axisymmetric convergent-divergent nozzle with post-exit vanes installed for multiaxis thrust vectoring. The test was conducted at nozzle pressure ratios from 1.6 to 6.0. The results of this investigation indicate the following conclusions:

1. The thrust-vectoring (flow-turning) capability of some of these post-exit-vane configurations was competitive with other multiaxis thrust-vectoring concepts. However, all the present post-exit-vane configurations incurred large resultant gross-thrust losses to achieve vectored thrust. In general, any change in vane geometry which produced larger thrust-vector angles also caused larger resultant thrust losses.
2. Four post-exit vanes provided a much larger thrust-vector envelope than three post-exit vanes. Also, the three-vane configuration had an asymmetric thrust-vector envelope which depended on vane orientation around the nozzle exit.
3. Resultant vector angle was increased by moving the vane hinge toward the nozzle exhaust flow; axial location of the vane hinge had little effect on resultant thrust-vector angle.
4. Double-curvature ("spoon" shaped) vanes produced larger thrust-vector angles than single-curvature vanes.

NASA Langley Research Center
Hampton, Virginia 23665-5225
February 24, 1988

References

1. Capone, Francis J.: Summary of Propulsive-Lift Research in the Langley 16-Ft. Transonic Tunnel. *J. Aircr.*, vol. 13, no. 10, Oct. 1976, pp. 803–808.
2. Berrier, Bobby L.; Palcza, J. Lawrence; and Richey, G. Keith: Nonaxisymmetric Nozzle Technology Program—An Overview. AIAA Paper 77-1225, Aug. 1977.
3. Hiley, P. E.; Wallace, H. W.; and Booz, D. E.: Study of Non-Axisymmetric Nozzles Installed in Advanced Fighter Aircraft. AIAA Paper No. 75-1316, Sept.–Oct. 1975.
4. Lander, J. A.; and Palcza, J. Lawrence: Exhaust Nozzle Deflector Systems for V/STOL Fighter Aircraft. AIAA Paper No. 74-1169, Oct. 1974.
5. Wasson, H. R.; Hall, G. R.; and Palcza, J. L.: Results of a Feasibility Study To Add Canards and ADEN Nozzle to the YF-17. AIAA Paper No. 77-1227, Aug. 1977.
6. Berrier, B. L.; and Re, R. J.: A Review of Thrust-Vectoring Schemes for Fighter Aircraft. AIAA Paper No. 78-1023, July 1978.
7. Capone, Francis J.: The Nonaxisymmetric Nozzle—It Is for Real. AIAA Paper No. 79-1810, Aug. 1979.
8. Richey, G. K.; Surber, L. E.; and Berrier, B. L.: Airframe-Propulsion Integration for Fighter Aircraft. AIAA-83-0084, Jan. 1983.
9. Nelson, B. D.; and Nicolai, L. M.: Application of Multi-Function Nozzles to Advanced Fighters. AIAA-81-2618, Dec. 1981.
10. Capone, Francis J.; and Maiden, Donald L.: *Performance of Twin Two-Dimensional Wedge Nozzles Including Thrust Vectoring and Reversing Effects at Speeds up to Mach 2.20.* NASA TN D-8449, 1977.
11. Capone, Francis J.: *Static Performance of Five Twin-Engine Nonaxisymmetric Nozzles With Vectoring and Reversing Capability.* NASA TP-1224, 1978.
12. *F-15 2-D Nozzle System Integration Study. Volume I—Technical Report.* NASA CR-145295, 1978.
13. Berrier, Bobby L.; and Re, Richard J.: *Effect of Several Geometric Parameters on the Static Internal Performance of Three Nonaxisymmetric Nozzle Concepts.* NASA TP-1468, 1979.
14. Capone, Francis J.; and Berrier, Bobby L.: *Investigation of Axisymmetric and Nonaxisymmetric Nozzles Installed on a 0.10-Scale F-18 Prototype Airplane Model.* NASA TP-1638, 1980.
15. Herbst, W.: Future Fighter Technologies. *J. Aircr.*, vol. 17, no. 8, Aug. 1980, pp. 561–566.
16. Lacey, David W.: Air Combat Advantages From Reaction Control Systems. SAE Tech. Paper Ser. 801177, Oct. 1980.
17. White, S. N.: *Feasibility Study for Integrating Thrust Vectoring as Primary Flight Control System.* NASA CR-165758, 1981.
18. Kraus, W.; Przibilla, H.; and Haux, U.: Stability and Control for High Angle of Attack Maneuvering. *Criteria for Handling Qualities of Military Aircraft,* AGARD-CP-333, June 1982, pp. 15-1–15-11.
19. Herbst, W. B.: Supermaneuverability. *Workshop on Unsteady Separated Flow,* Michael S. Francis and Marvin W. Luttges, eds., AFOSR-TR-84-0911, U.S. Air Force, May 1984, pp. 1–9. (Available from DTIC as AD P004 153.)
20. Joshi, Dinesh S.; Shaw, Peter D.; Hodgkinson, John; Rock, Steven M.; Vincent, James H.; and Fisk, William S.: A Design Approach to Integrated Flight and Propulsion Control. SAE Tech. Paper Ser. 831482, Oct. 1983.
21. Hienz, Egon; and Vedova, Ralph: Requirements, Definition and Preliminary Design for an Axisymmetric Vectoring Nozzle, To Enhance Aircraft Maneuverability. AIAA-84-1212, June 1984.
22. Miller, L. Earl: *Post Stall Maneuvers and Thrust Vectoring Performance Analysis.* AFWAL-TR-84-3109, U.S. Air Force, July 1984. (Available from DTIC as AD A158 100.)
23. Herrick, Paul W.: Propulsion Influences on Air Combat. AIAA-85-1457, July 1985.
24. Gallaway, C. R.; and Osborn, R. F.: Aerodynamics Perspective of Supermaneuverability. AIAA-85-4068, Oct. 1985.
25. Lacey, David W.; and Murphy, Richard D.: *Jet Engine Thrust Turning by the Use of Small Externally Mounted Vanes.* DTNSRDC-82/080, U.S. Navy, Jan. 1983. (Available from DTIC as AD B070 970L.)
26. Mason, Mary L.; and Berrier, Bobby L.: *Static Investigation of Several Yaw Vectoring Concepts on Nonaxisymmetric Nozzles.* NASA TP-2432, 1985.
27. Capone, Francis J.; and Mason, Mary L.: *Multiaxis Aircraft Control Power From Thrust Vectoring at High Angles of Attack.* NASA TM-87741, 1986.
28. Peddrew, Kathryn H., compiler: *A User's Guide to the Langley 16-Foot Transonic Tunnel.* NASA TM-83186, 1981.
29. Berrier, Bobby L.; Leavitt, Laurence D.; and Bangert, Linda S.: *Operating Characteristics of the Multiple Critical Venturi System and Secondary Calibration Nozzles Used for Weight-Flow Measurements in the Langley 16-Foot Transonic Tunnel.* NASA TM-86405, 1985.
30. Mercer, Charles E.; Berrier, Bobby L.; Capone, Francis J.; Grayston, Alan M.; and Sherman, C. D.: *Computations for the 16-Foot Transonic Tunnel—NASA, Langley Research Center. Revision 1.* NASA TM-86319, 1987.
31. Berrier, Bobby L.; and Re, Richard J.: *Investigation of Convergent-Divergent Nozzles Applicable to Reduced-Power Supersonic Cruise Aircraft.* NASA TP-1766, 1980.
32. Mason, Mary L.; and Berrier, Bobby L.: *Static Performance of Nonaxisymmetric Nozzles With Yaw Thrust-Vectoring Vanes.* NASA TP-2813, 1988.

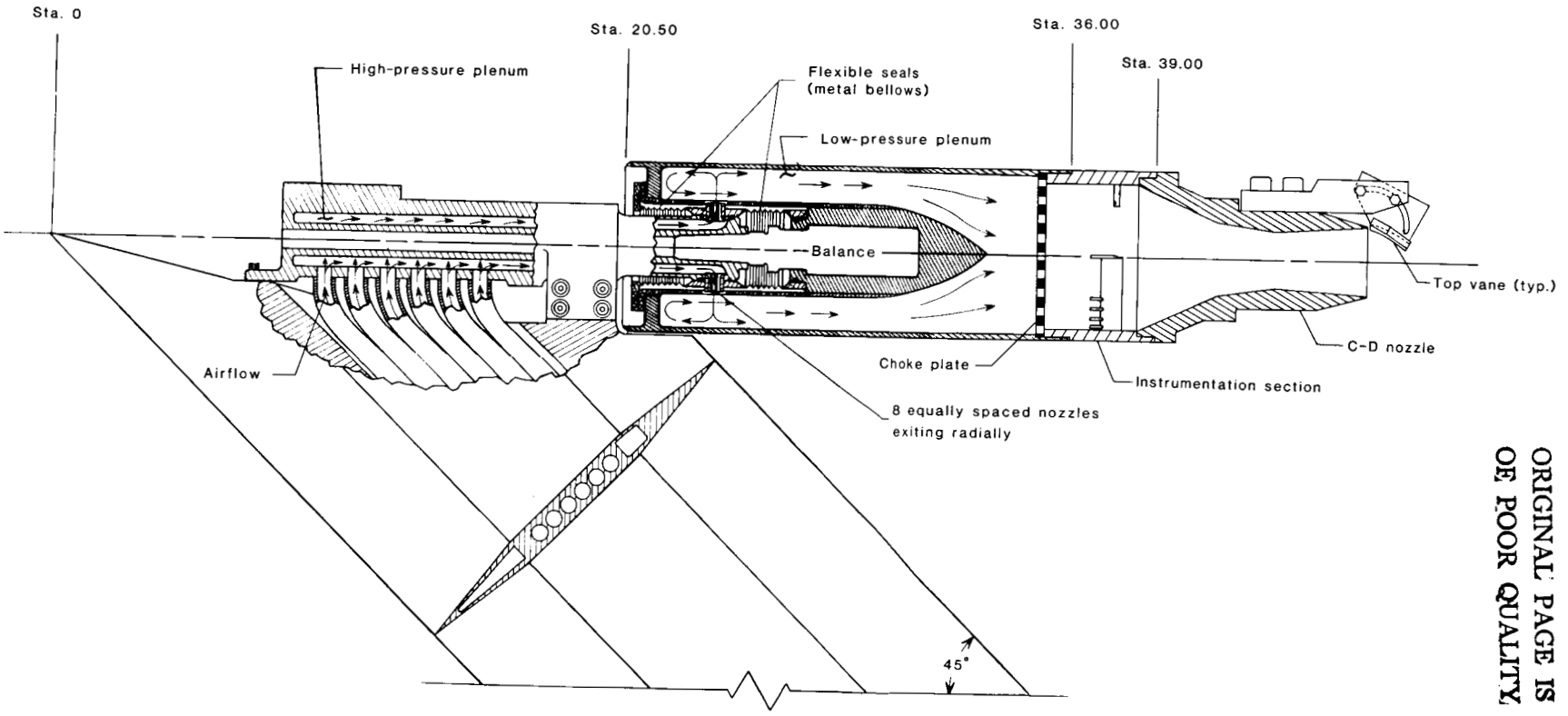

Figure 1. Sketch of C-D nozzle installation on high-pressure air propulsion-simulation hardware. Only the top thrust deflector vane is shown. All dimensions are in inches unless otherwise noted.

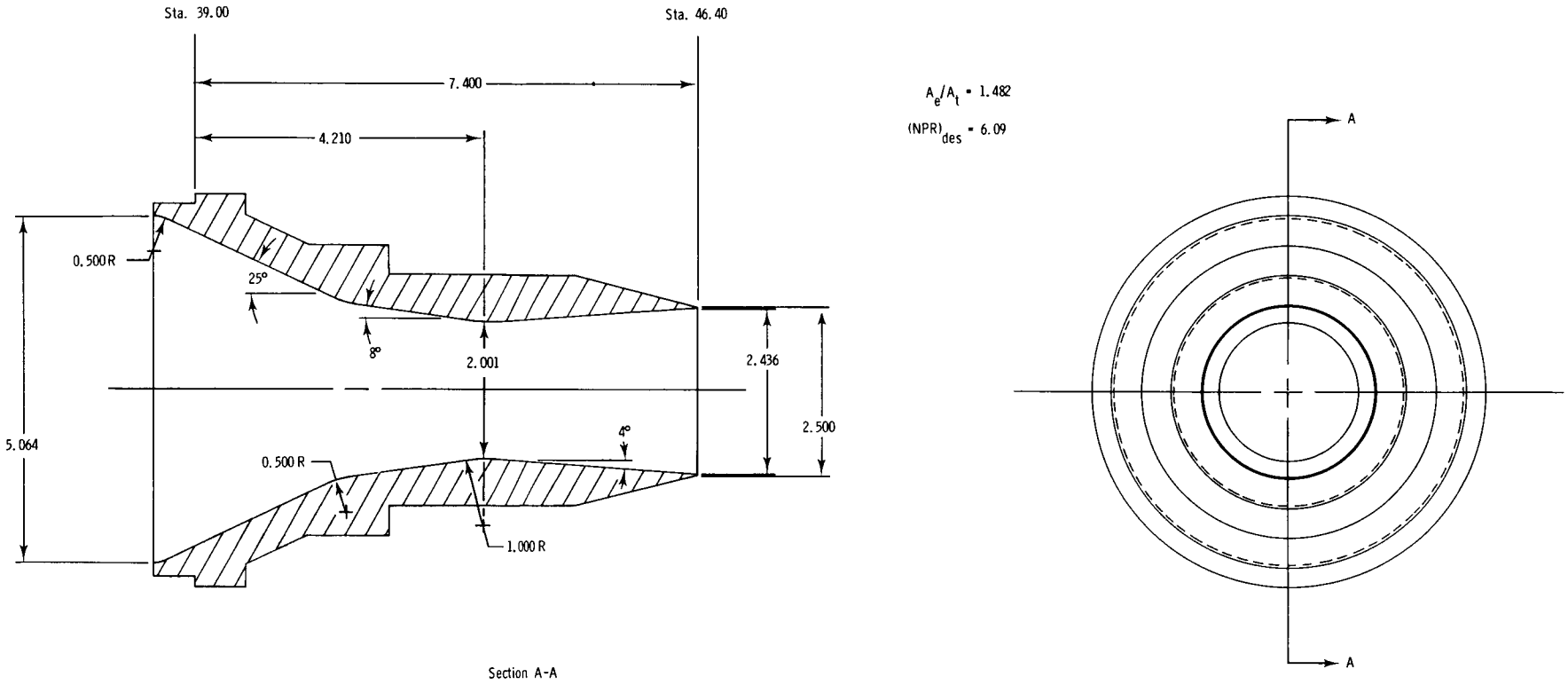

Figure 2. Sketch showing important geometry details of the axisymmetric convergent-divergent nozzle. All dimensions are in inches unless otherwise noted.

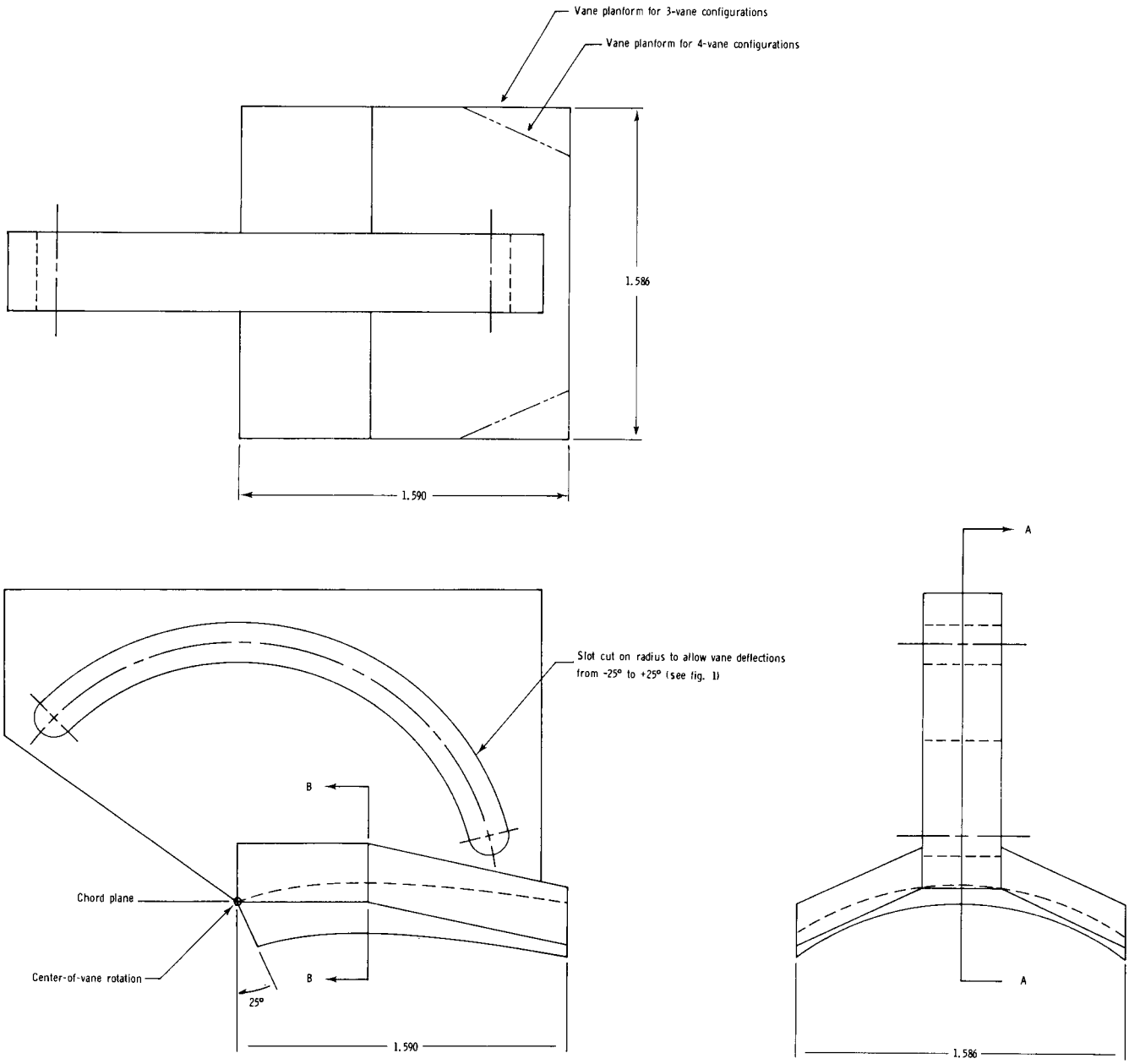

(a) Thrust deflector vane planform definition.

Figure 3. Sketches showing geometry of thrust deflector vanes. All dimensions are in inches unless otherwise noted.

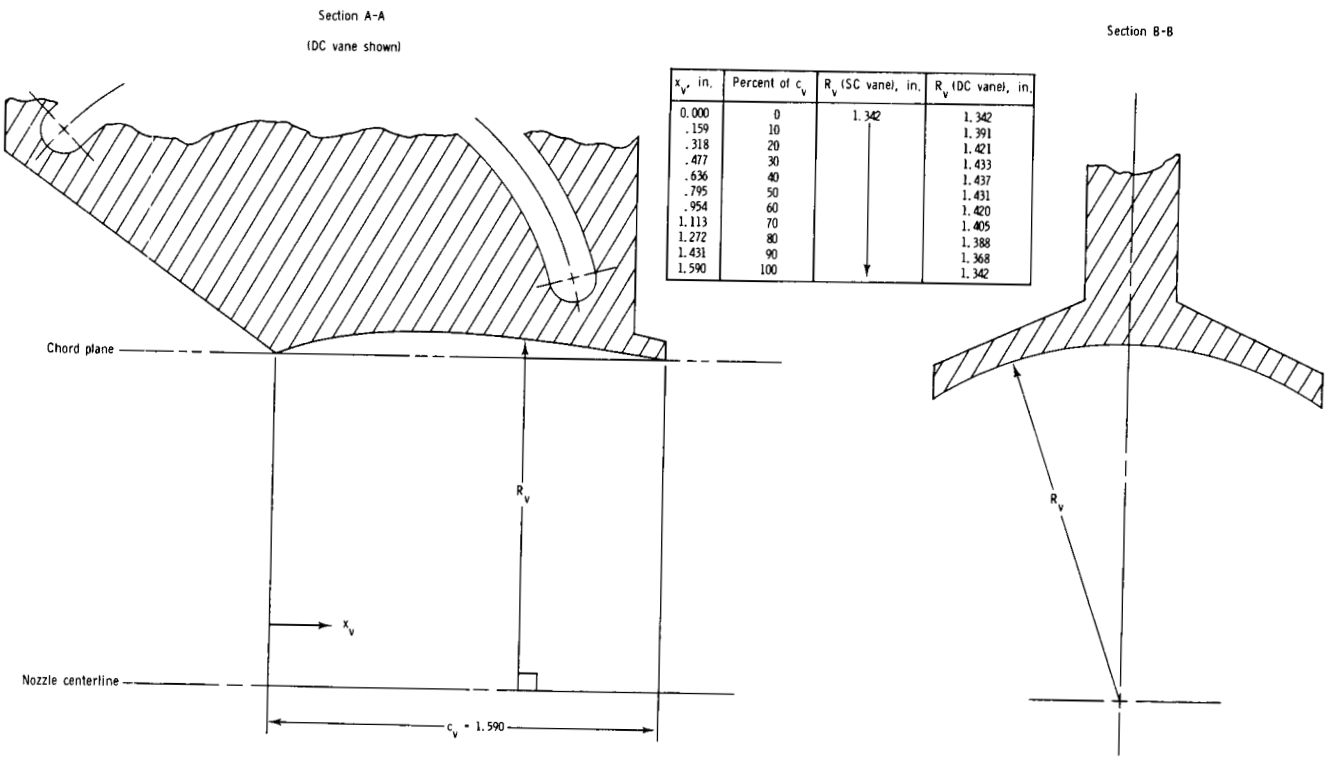

x_v, in.	Percent of c_v	R_v (SC vane), in.	R_v (DC vane), in.
0.000	0	1.342	1.342
.159	10		1.391
.318	20		1.421
.477	30		1.433
.636	40		1.437
.795	50		1.431
.954	60		1.420
1.113	70		1.405
1.272	80		1.388
1.431	90		1.368
1.590	100		1.342

(b) Thrust deflector vane curvature definition.

Figure 3. Concluded.

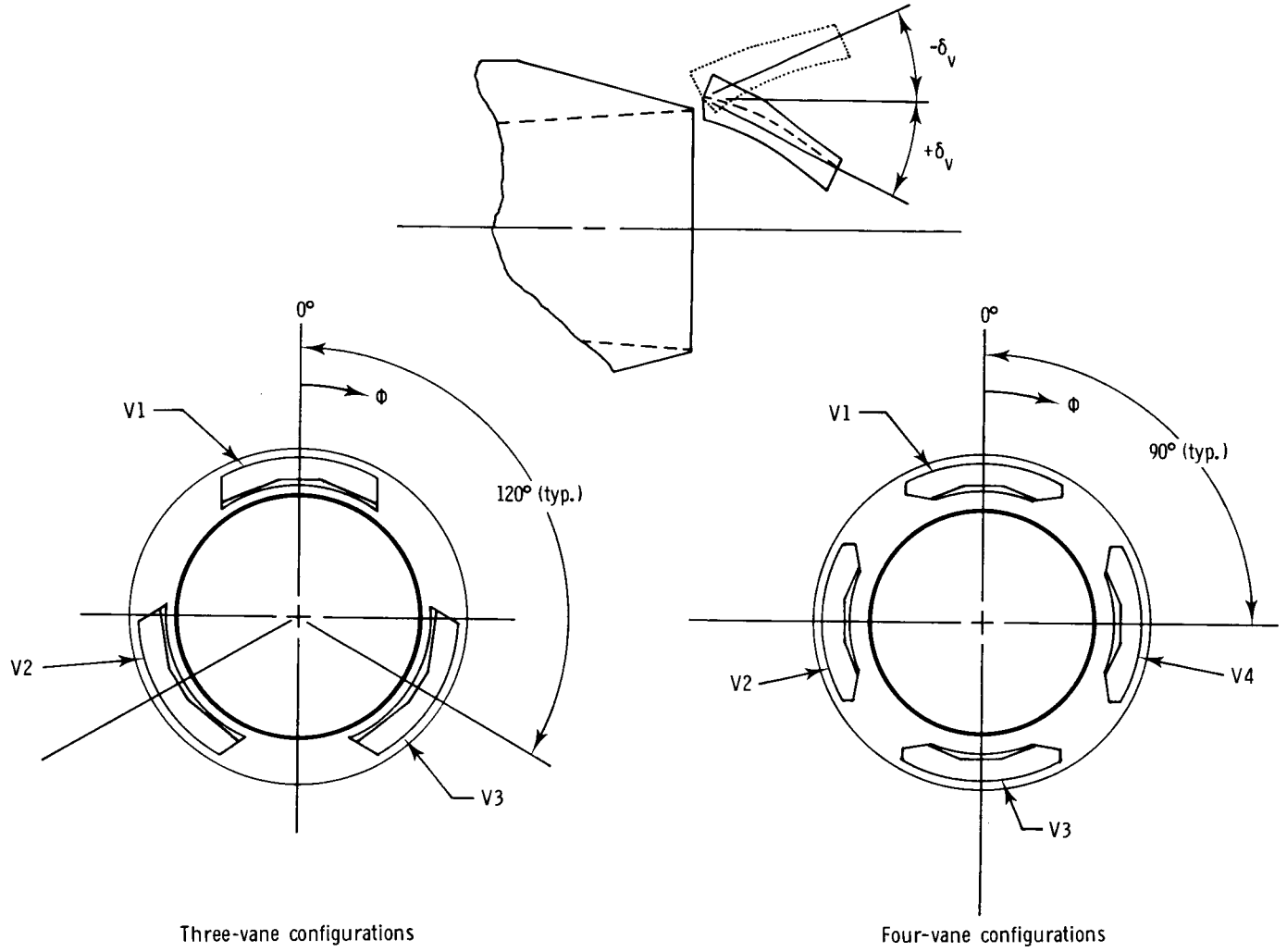

Vanes shown undeflected and with supports omitted for clarity

(a) Thrust deflector vane circumferential position.

Figure 4. Sketches showing thrust deflector vane position relative to C-D nozzle exit. All dimensions are in inches unless otherwise noted.

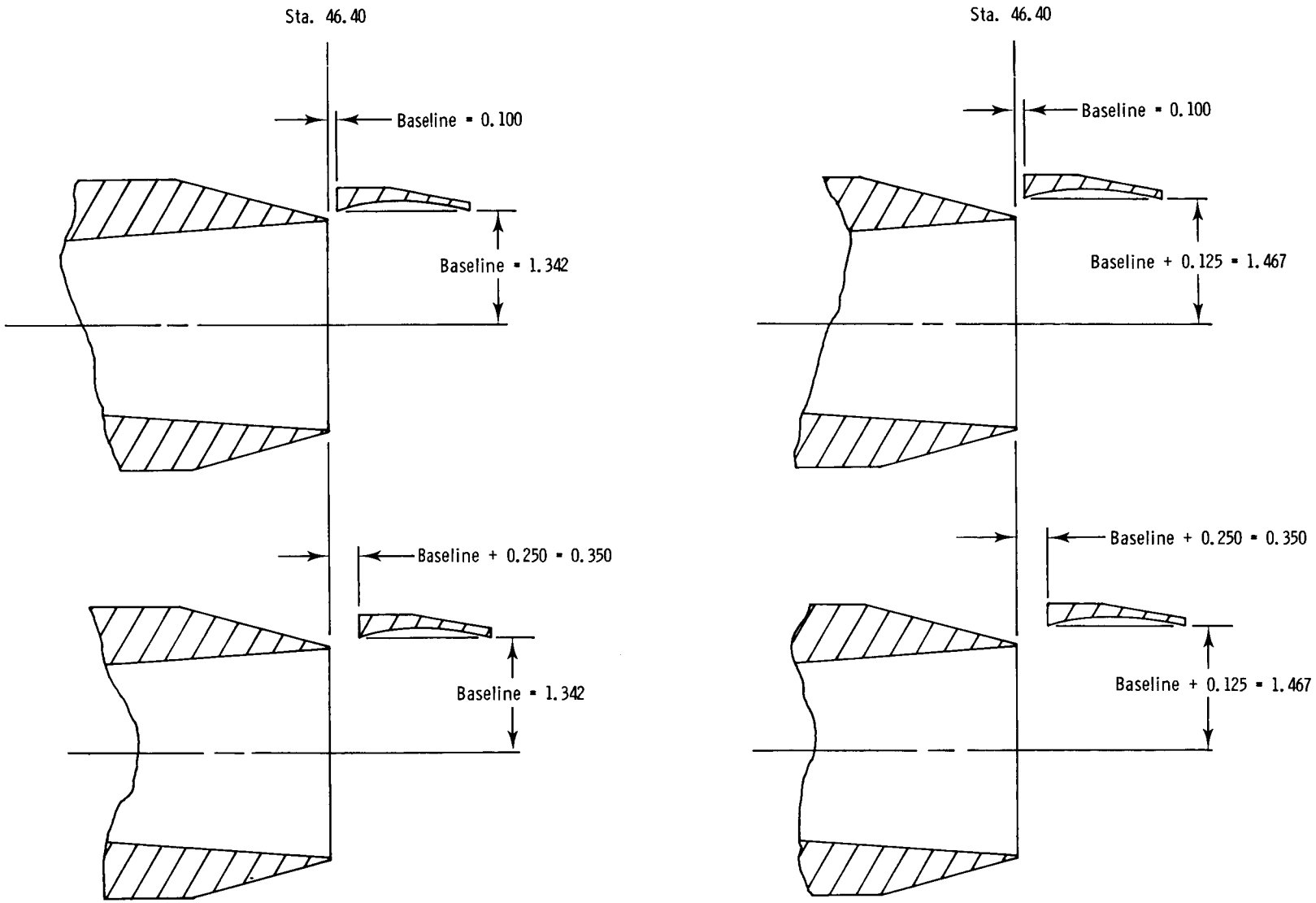

(b) Thrust deflector vane longitudinal and radial positions.

Figure 4. Concluded.

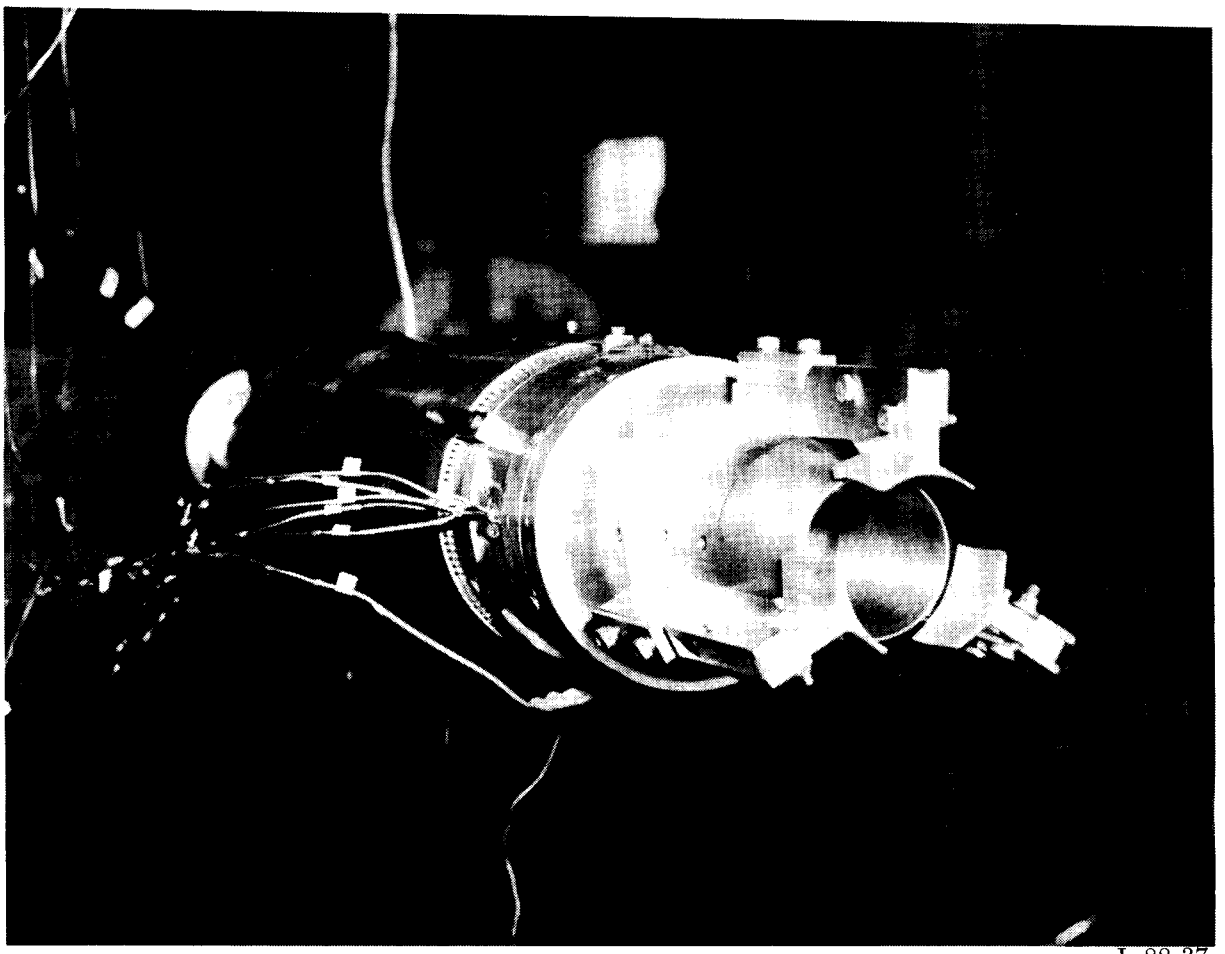

L-88-37

(a) $\delta_{v,V1} = \delta_{v,V2} = \delta_{v,V3} = 0°$.

Figure 5. Photographs of three-vane axisymmetric-nozzle configurations.

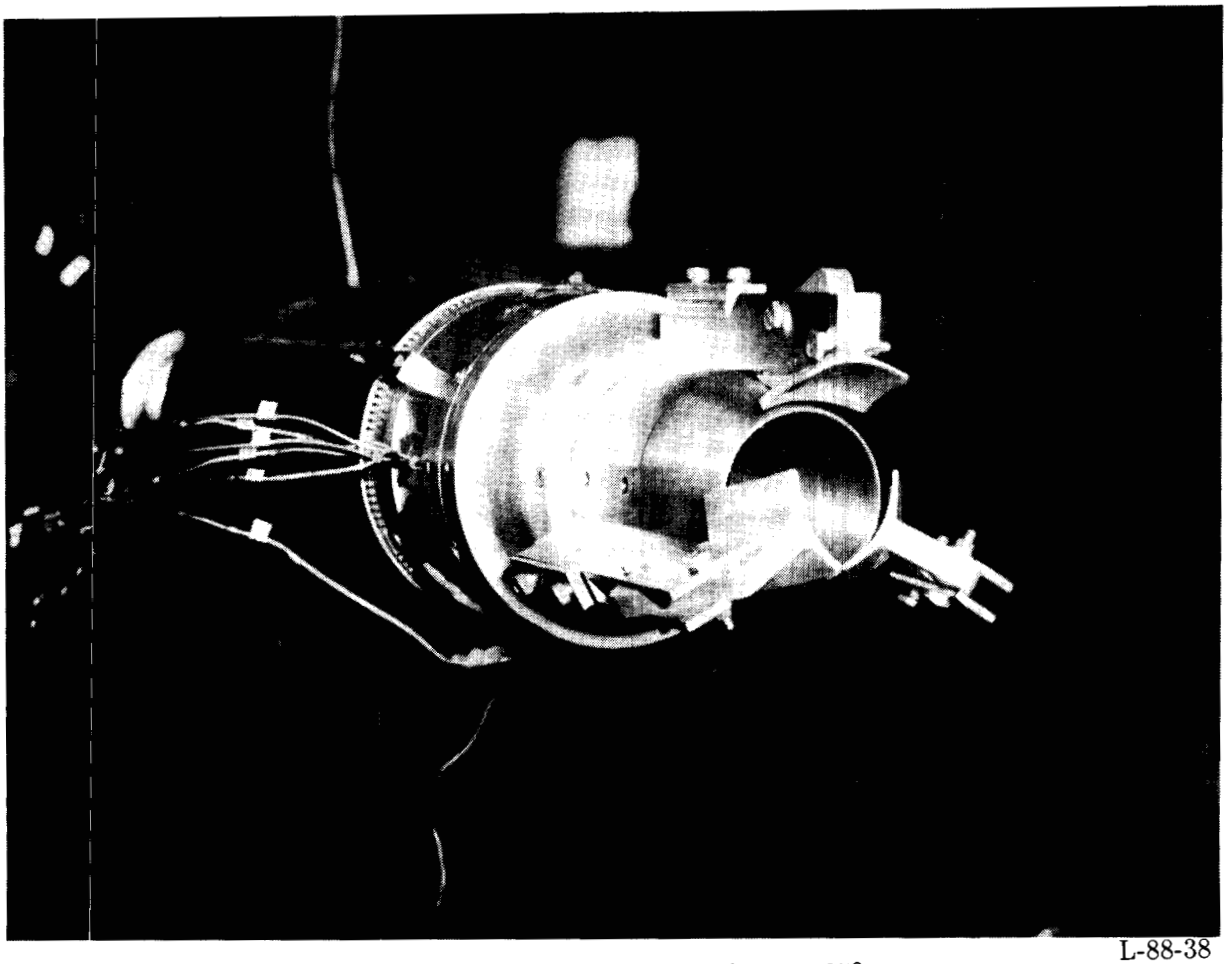

L-88-38

(b) $\delta_{v,V1} = -25°; \delta_{v,V2} = \delta_{v,V3} = 25°$.

Figure 5. Continued.

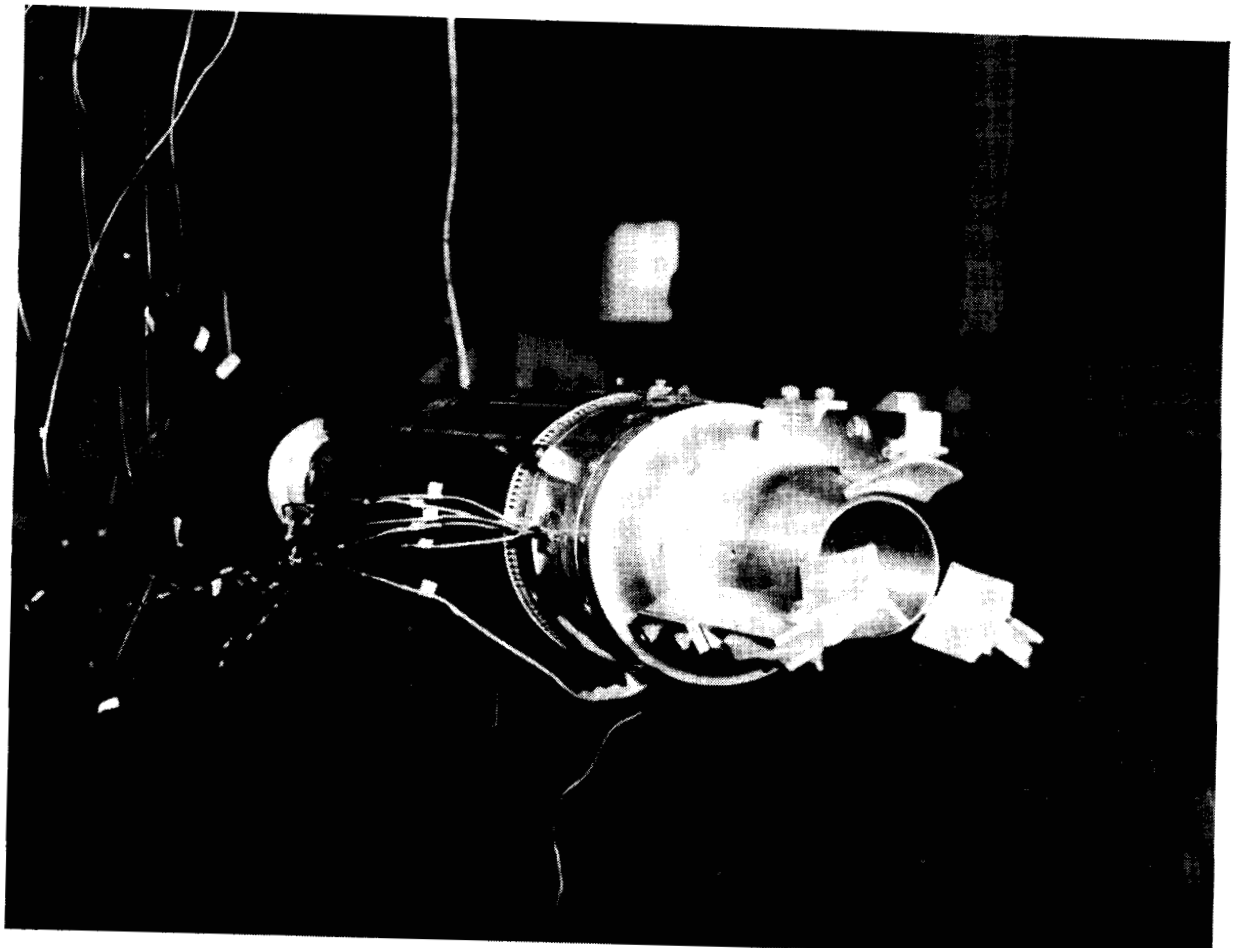

L-88-39

(c) $\delta_{v,V1} = -25°; \delta_{v,V2} = 25°; \delta_{v,V3} = -25°$.

Figure 5. Concluded.

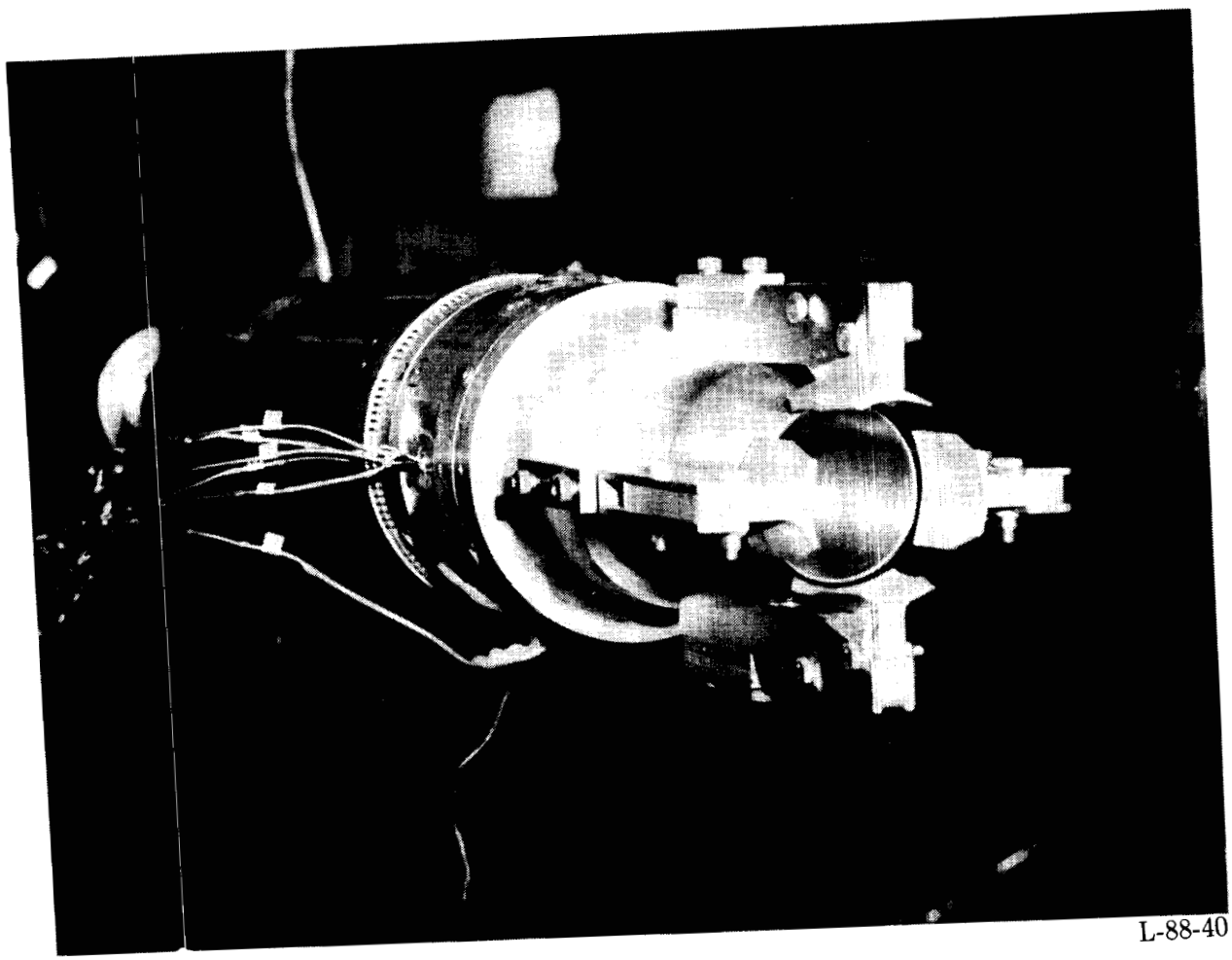

L-88-40

(a) $\delta_{v,V1} = \delta_{v,V2} = \delta_{v,V3} = \delta_{v,V4} = 0°$.

Figure 6. Photographs of four-vane axisymmetric-nozzle configurations.

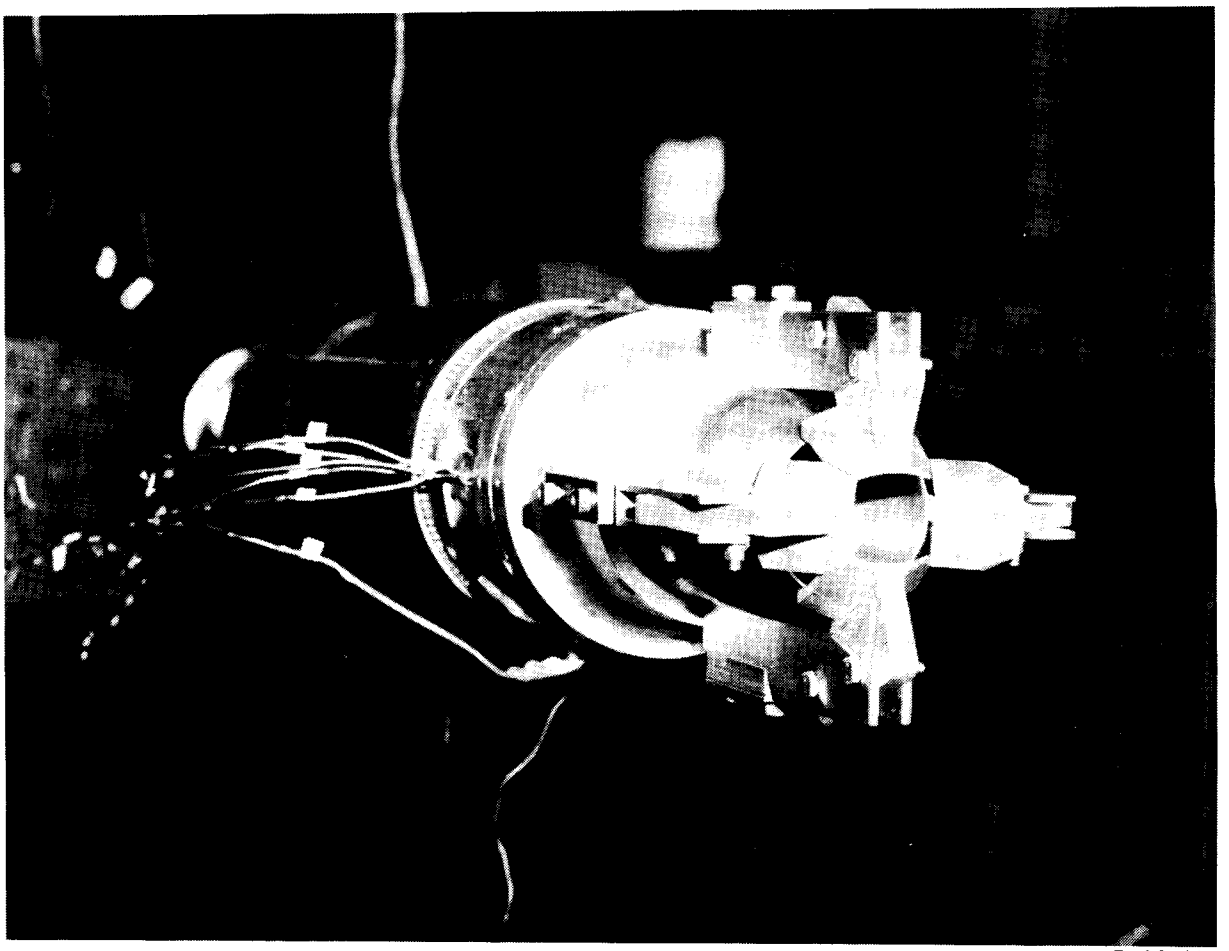

L-88-41

(b) $\delta_{v,V1} = \delta_{v,V2} = \delta_{v,V3} = 25°; \delta_{v,V4} = -25°$.

Figure 6. Continued.

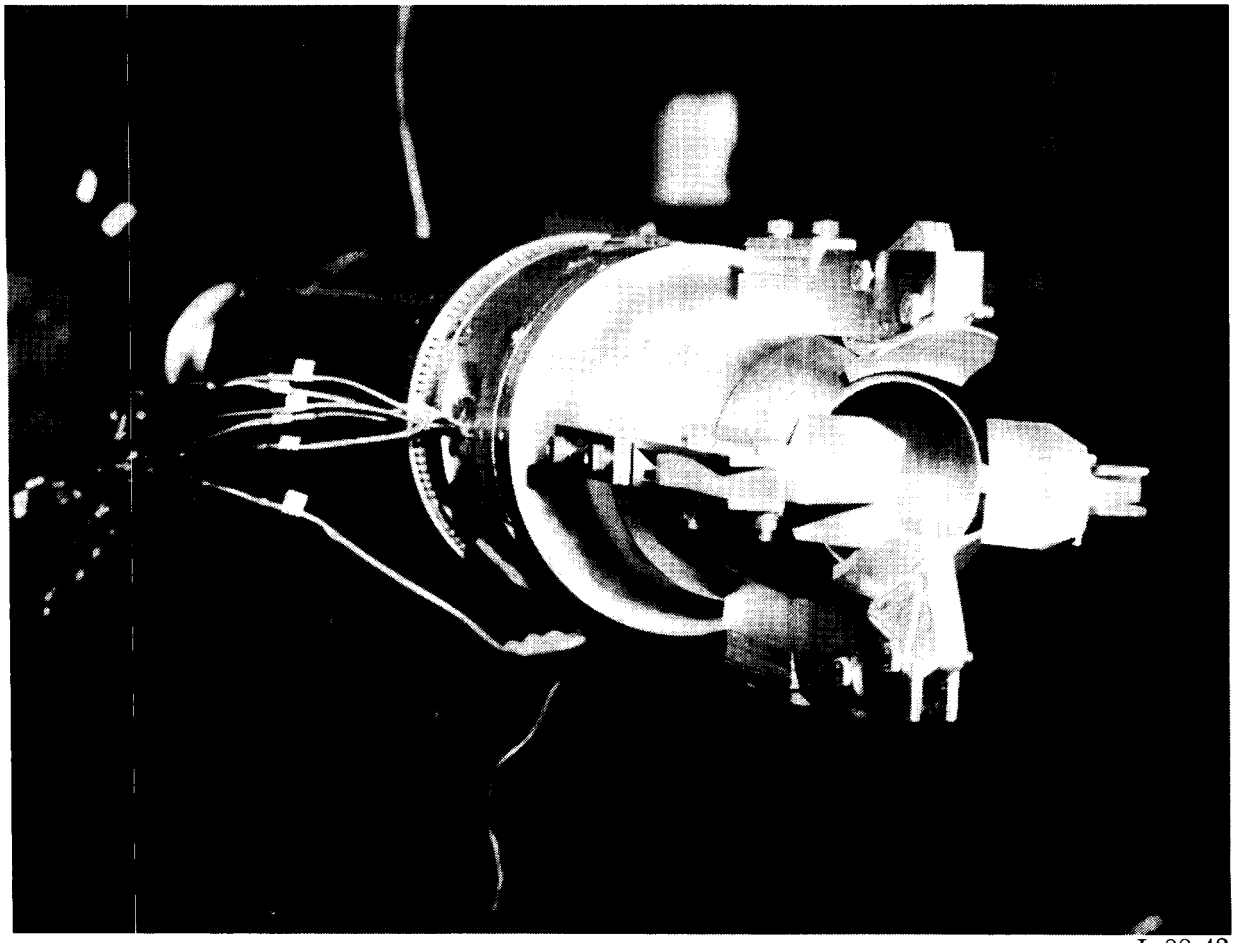

L-88-42

(c) $\delta_{v,V1} = -25°; \delta_{v,V2} = \delta_{v,V3} = 25°; \delta_{v,V4} = -25°$.

Figure 6. Concluded.

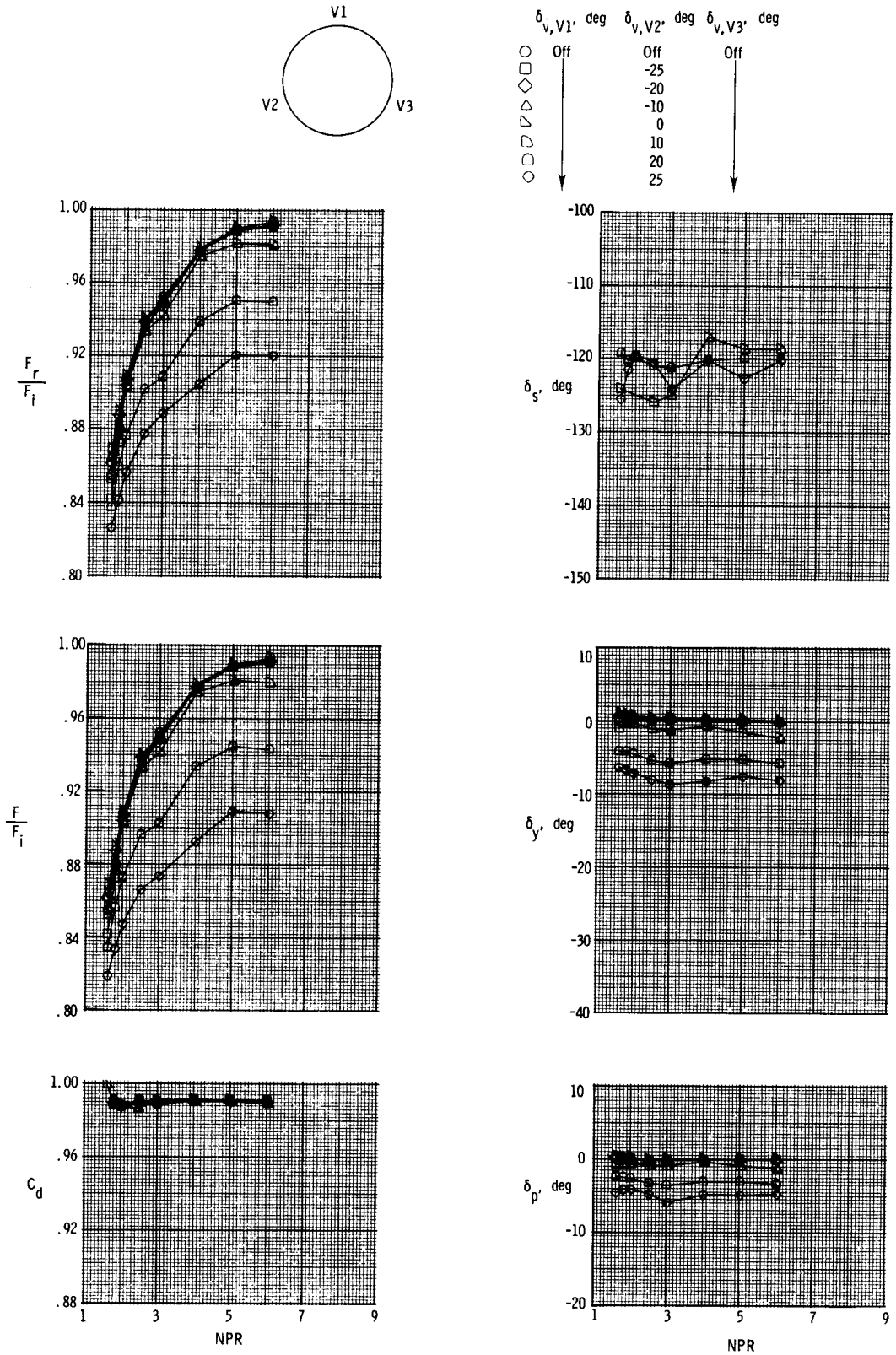

Figure 7. Effect of vane deflection on nozzle performance of axisymmetric nozzle with SC vanes; three-vane configurations.

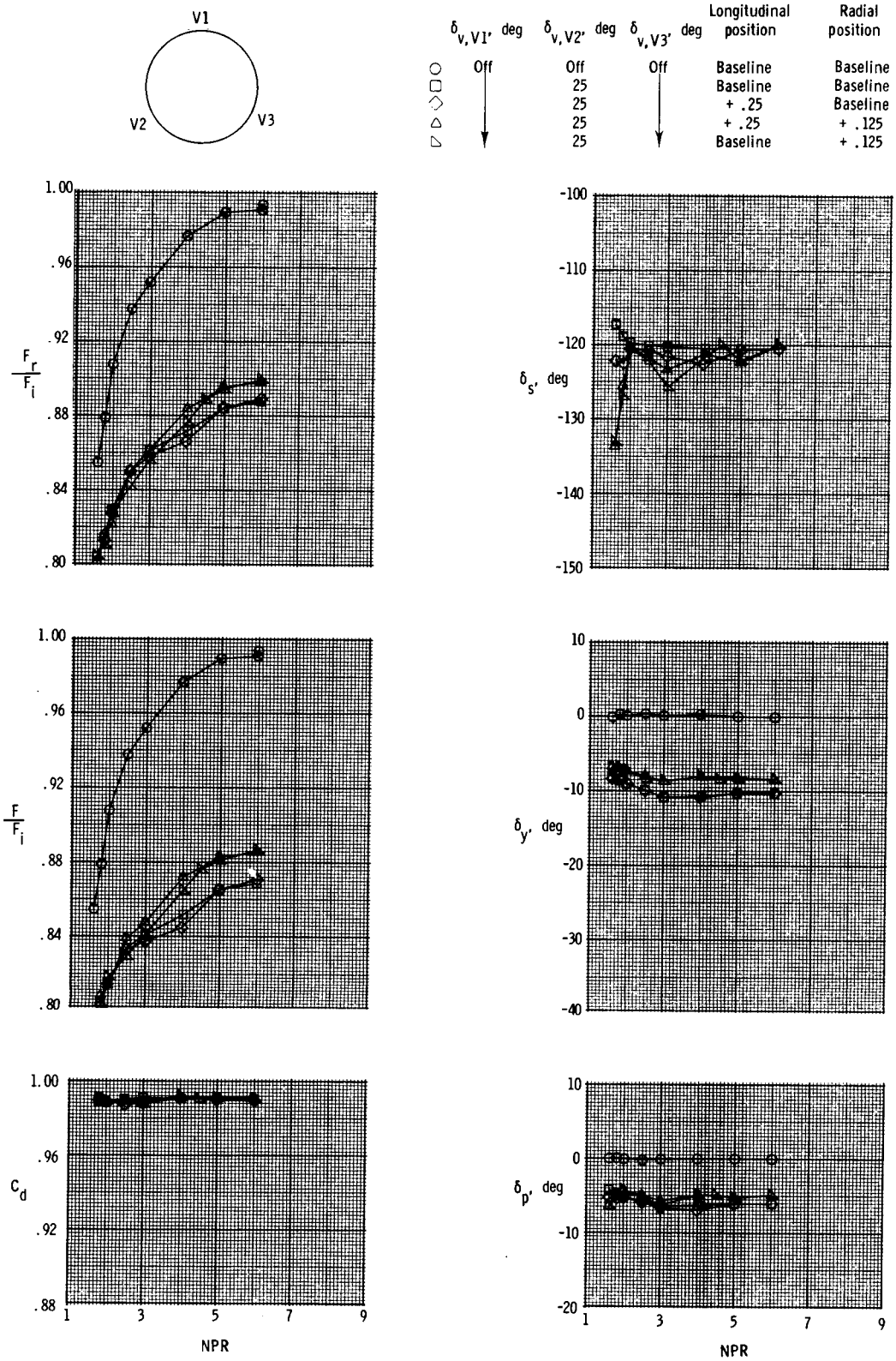

Figure 8. Effect of varying radial and longitudinal vane positions on nozzle performance of axisymmetric nozzle with DC vanes; three-vane configurations.

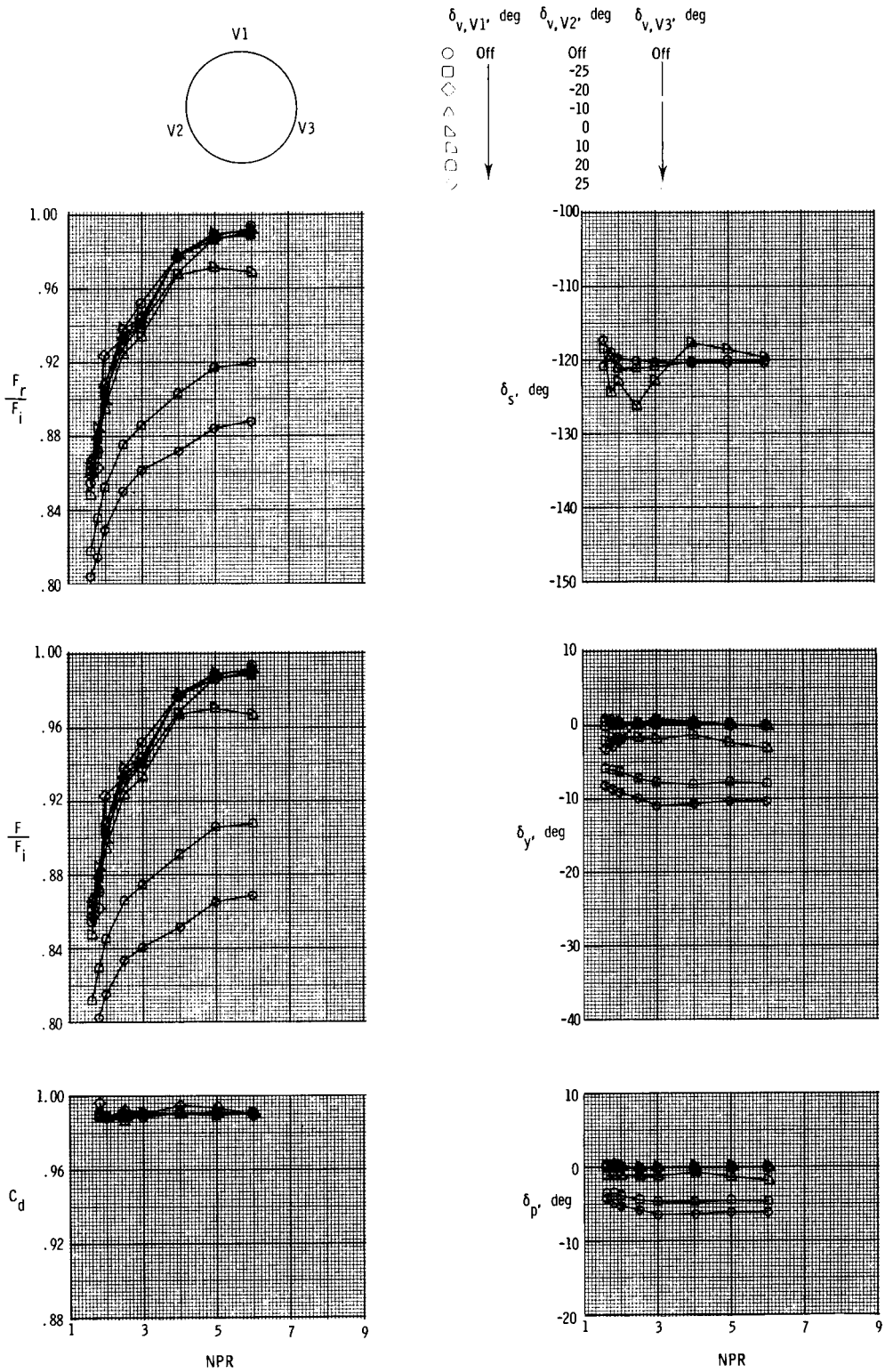

(a) $\delta_{v,V1} = \delta_{v,V3} =$ Off; vary $\delta_{v,V2}$.

Figure 9. Effect of vane deflection on nozzle performance of axisymmetric nozzle with DC vanes; three-vane configurations.

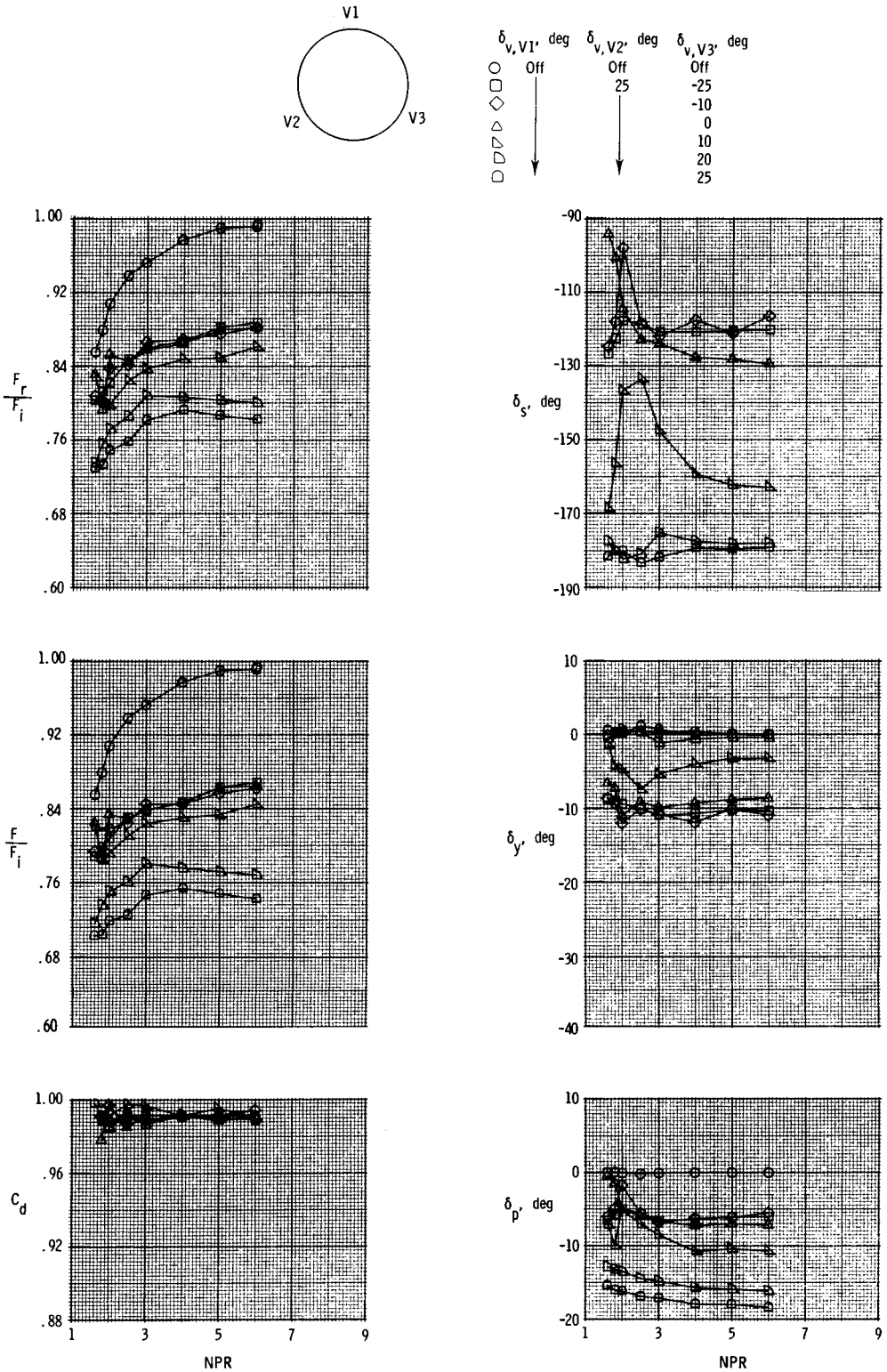

(b) $\delta_{v,V1}$ = Off; $\delta_{v,V2} = 25°$; vary $\delta_{v,V3}$.

Figure 9. Continued.

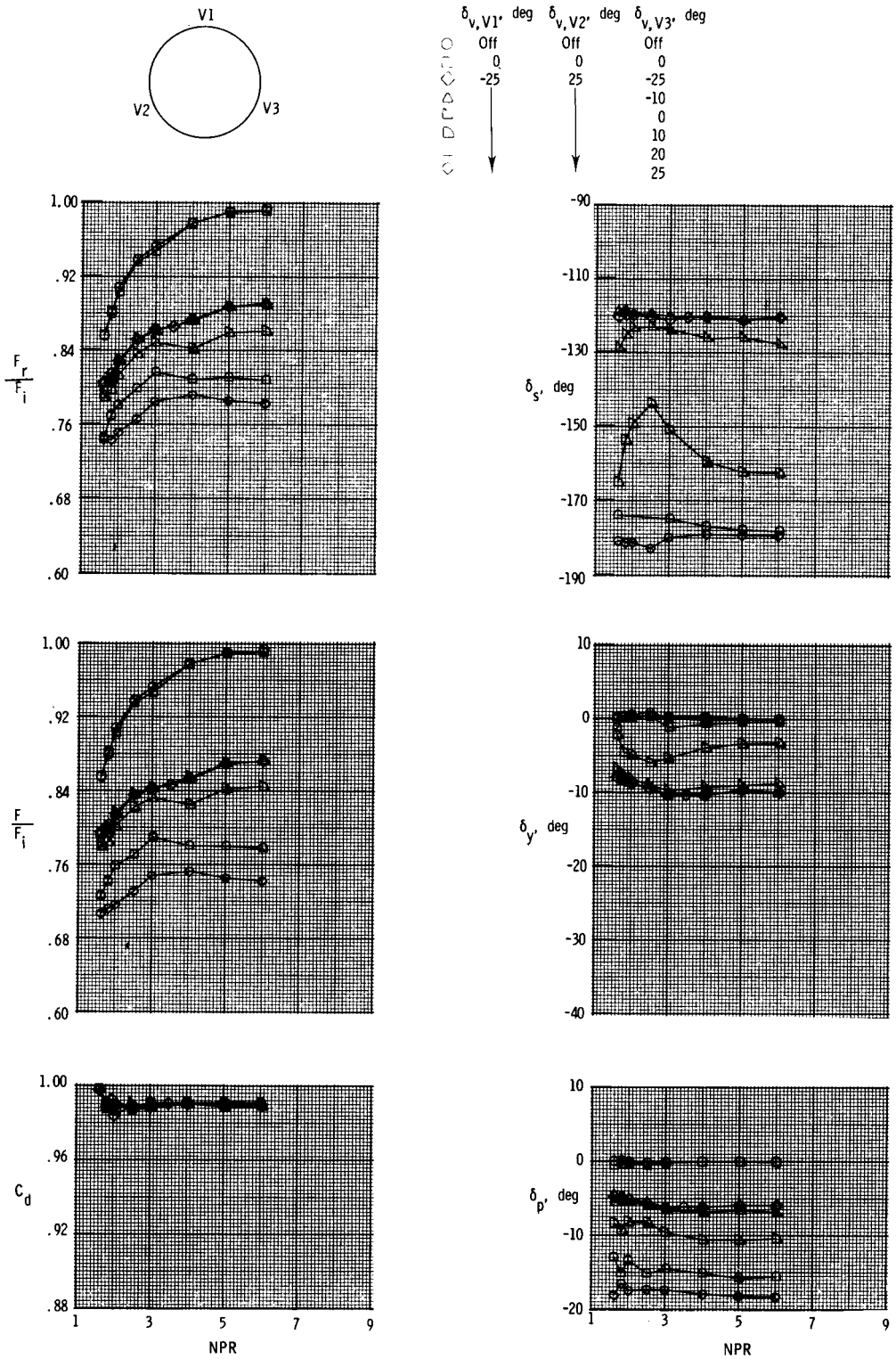

(c) $\delta_{v,V1} = -25°$; $\delta_{v,V2} = 25°$; vary $\delta_{v,V3}$.

Figure 9. Concluded.

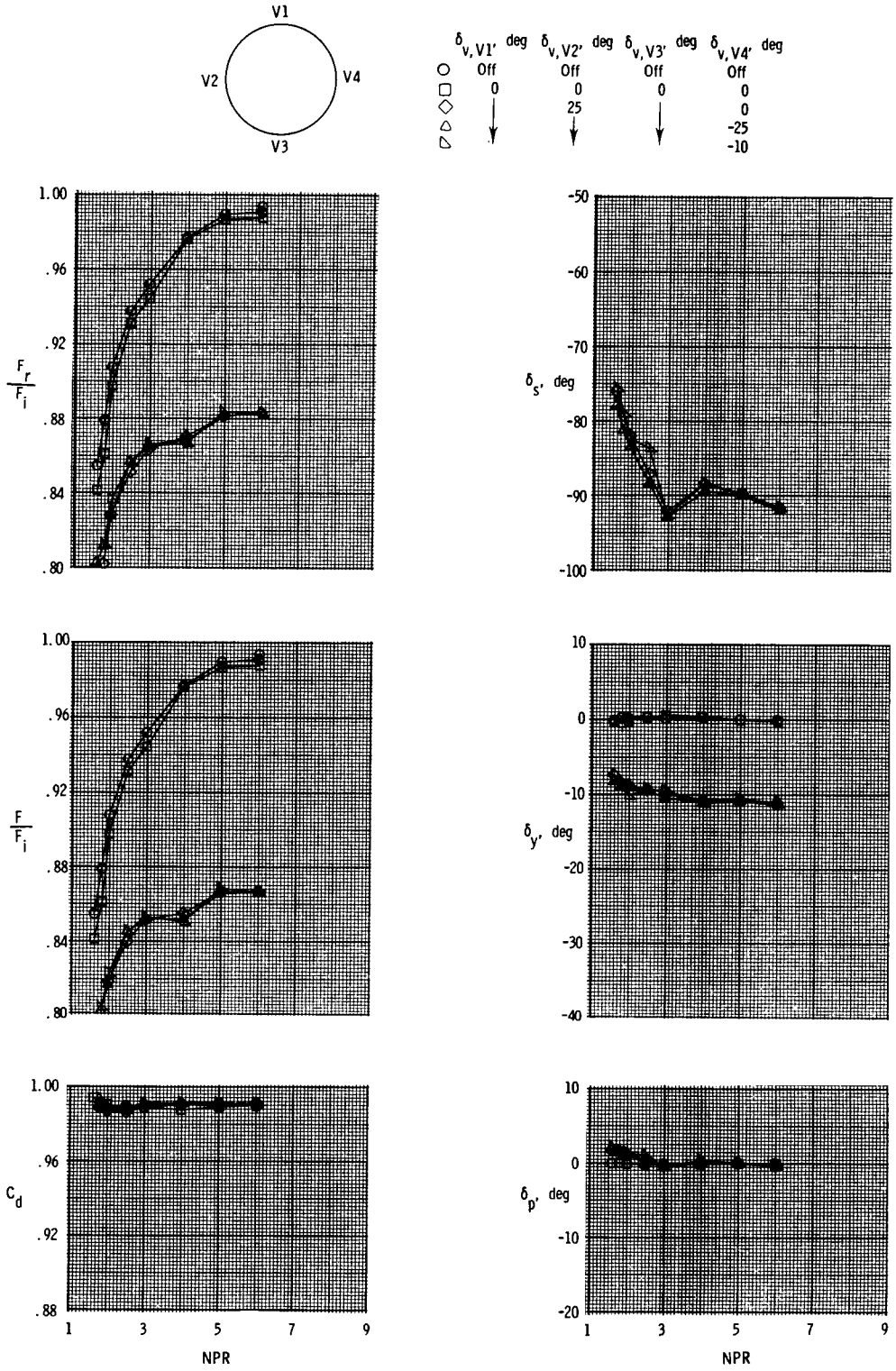

(a) $\delta_{v,V1} = \delta_{v,V3} = 0°$; $\delta_{v,V2} = 25°$; vary $\delta_{v,V4}$.

Figure 10. Effect of vane deflection on nozzle performance of axisymmetric nozzle with DC vanes; four-vane configurations.

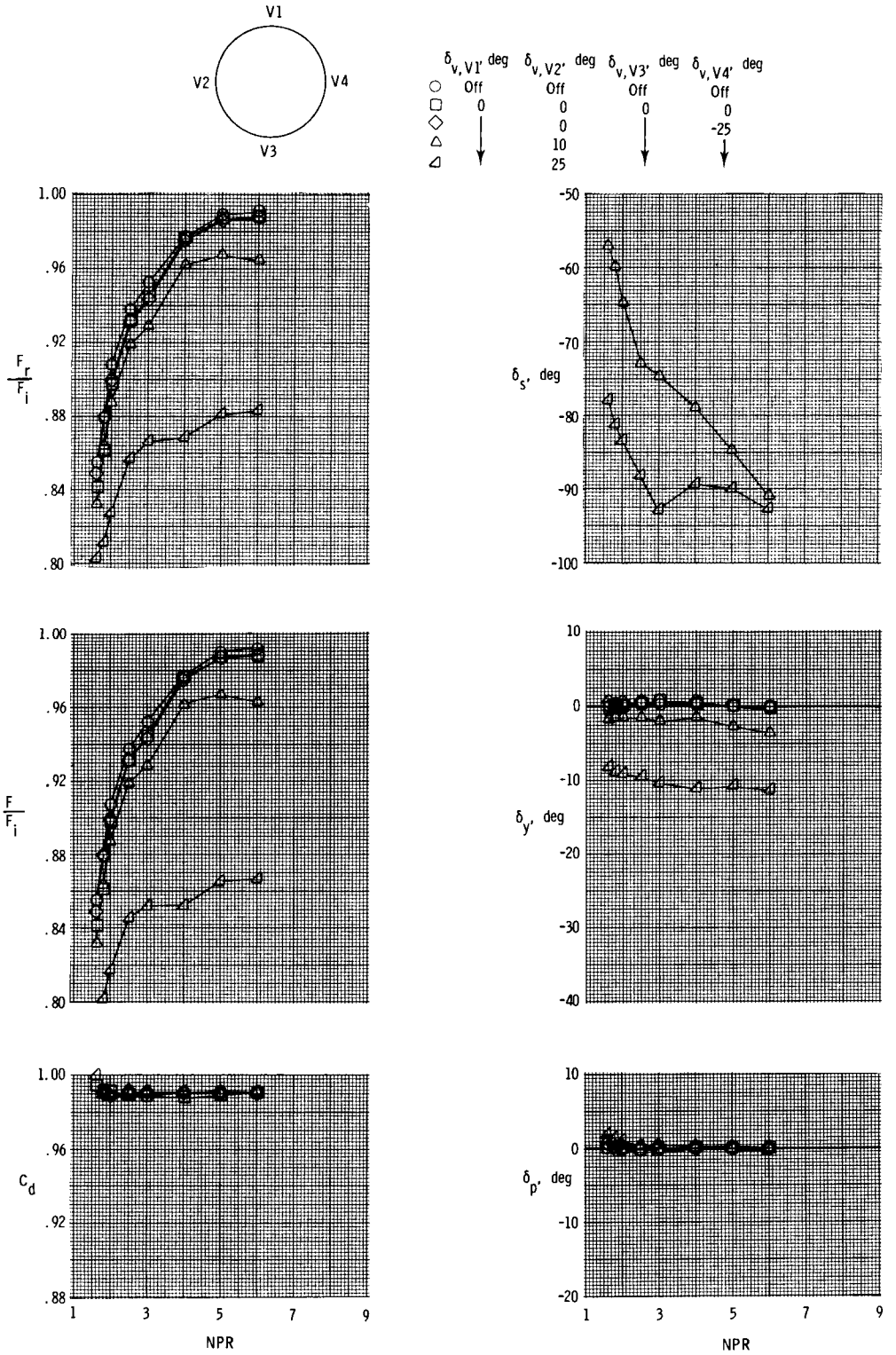

(b) $\delta_{v,V1} = \delta_{v,V3} = 0°$; $\delta_{v,V4} = -25°$; vary $\delta_{v,V2}$.

Figure 10. Continued.

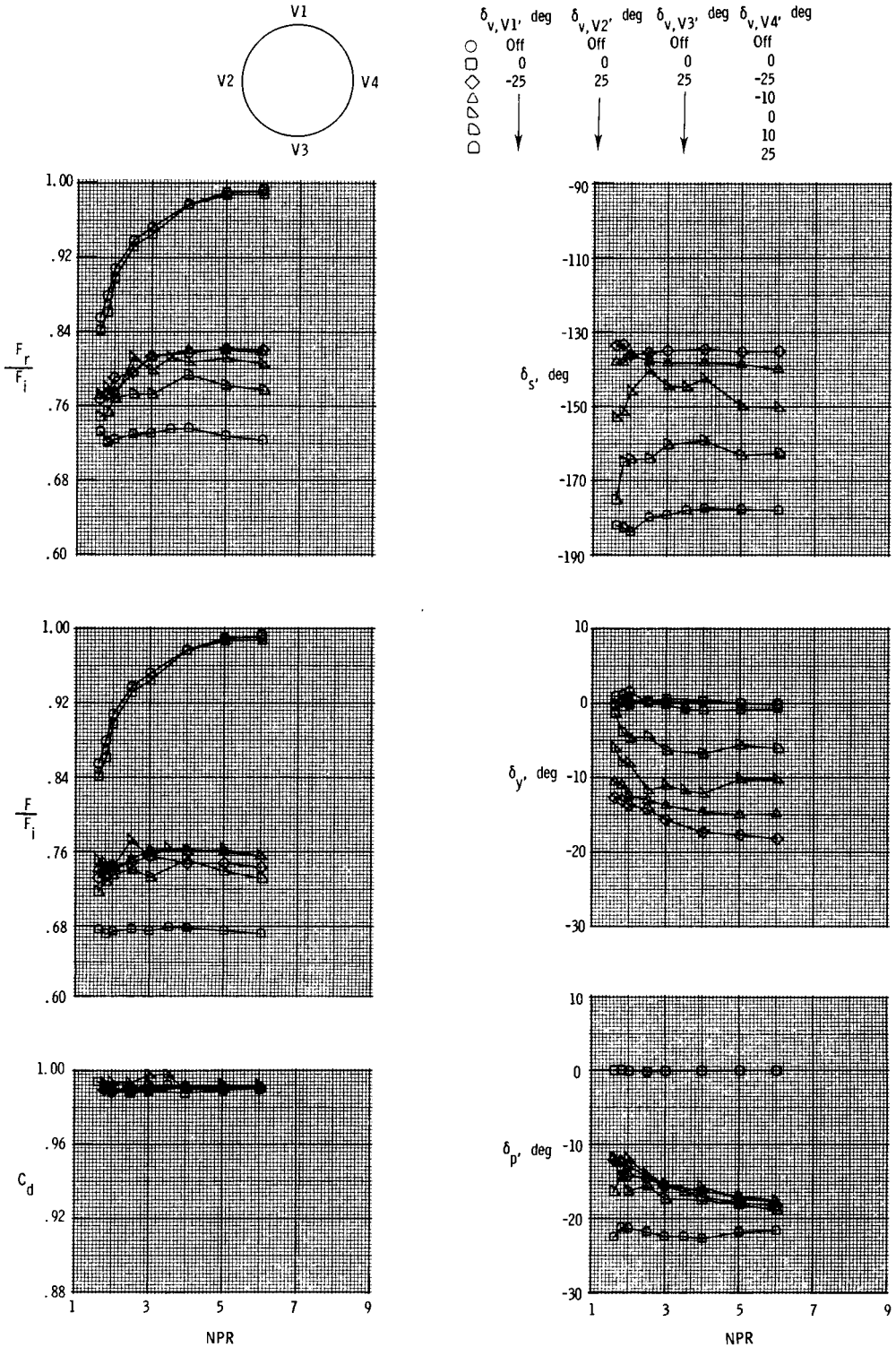

(c) $\delta_{v,V1} = -25°; \delta_{v,V2} = \delta_{v,V3} = 25°$; vary $\delta_{v,V4}$.

Figure 10. Continued.

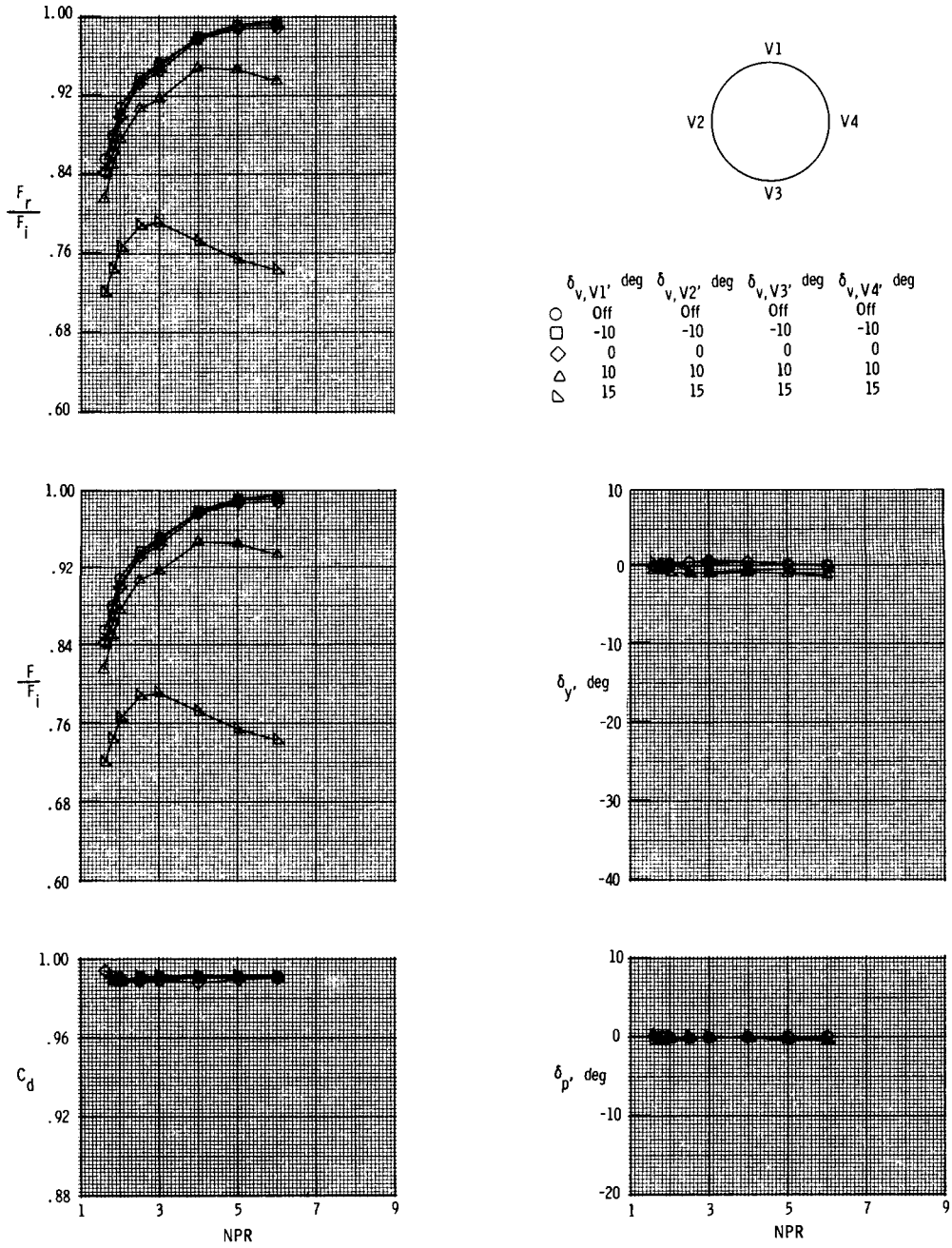

(d) $\delta_{v,V1} = \delta_{v,V2} = \delta_{v,V3} = \delta_{v,V4}$ = Variable.

Figure 10. Concluded.

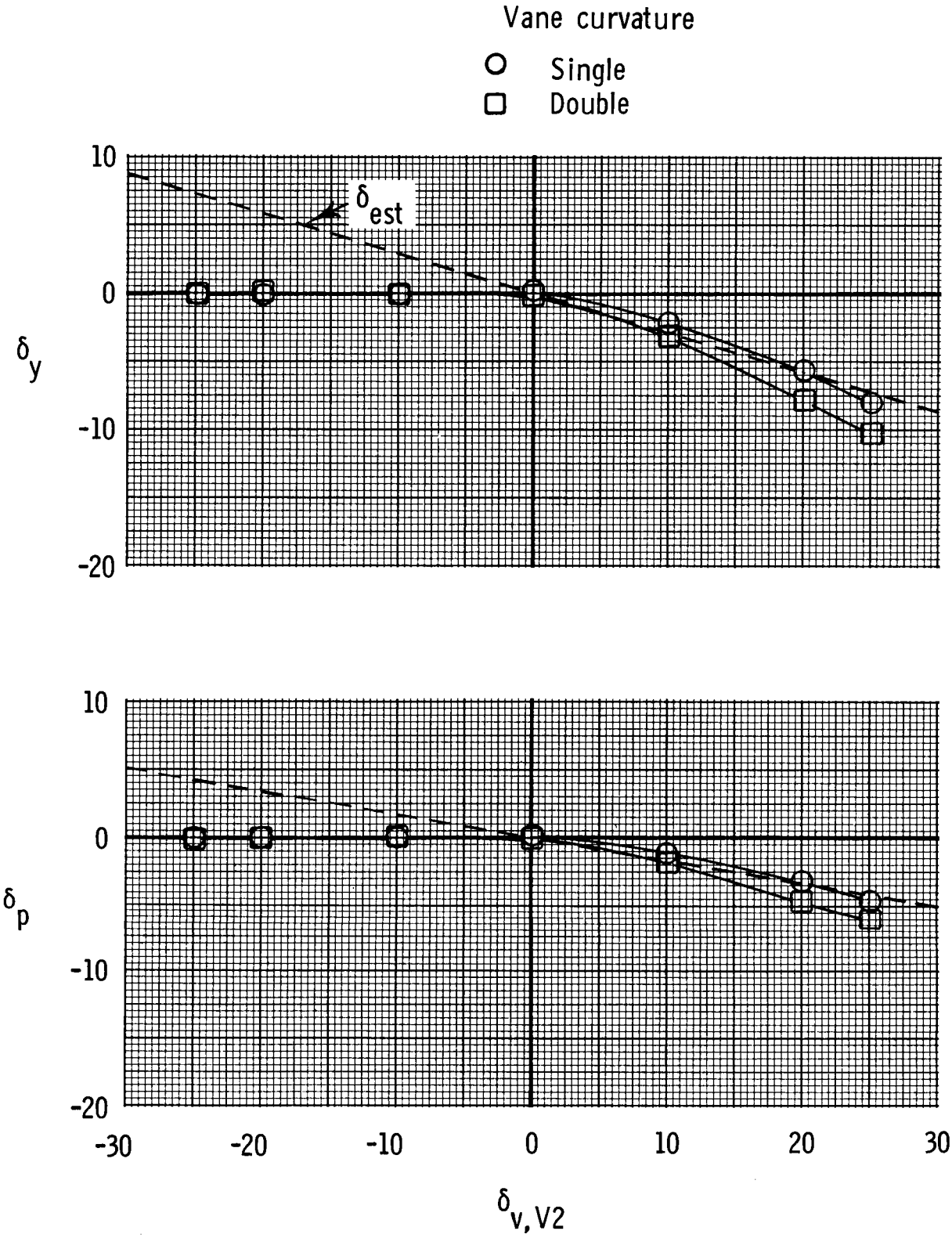

(a) Thrust-vector angles.

Figure 11. Effects of vane curvature on performance of axisymmetric nozzle with three vanes for thrust vectoring. $\delta_{v,V1} = \delta_{v,V3} =$ Off; NPR = 6.0.

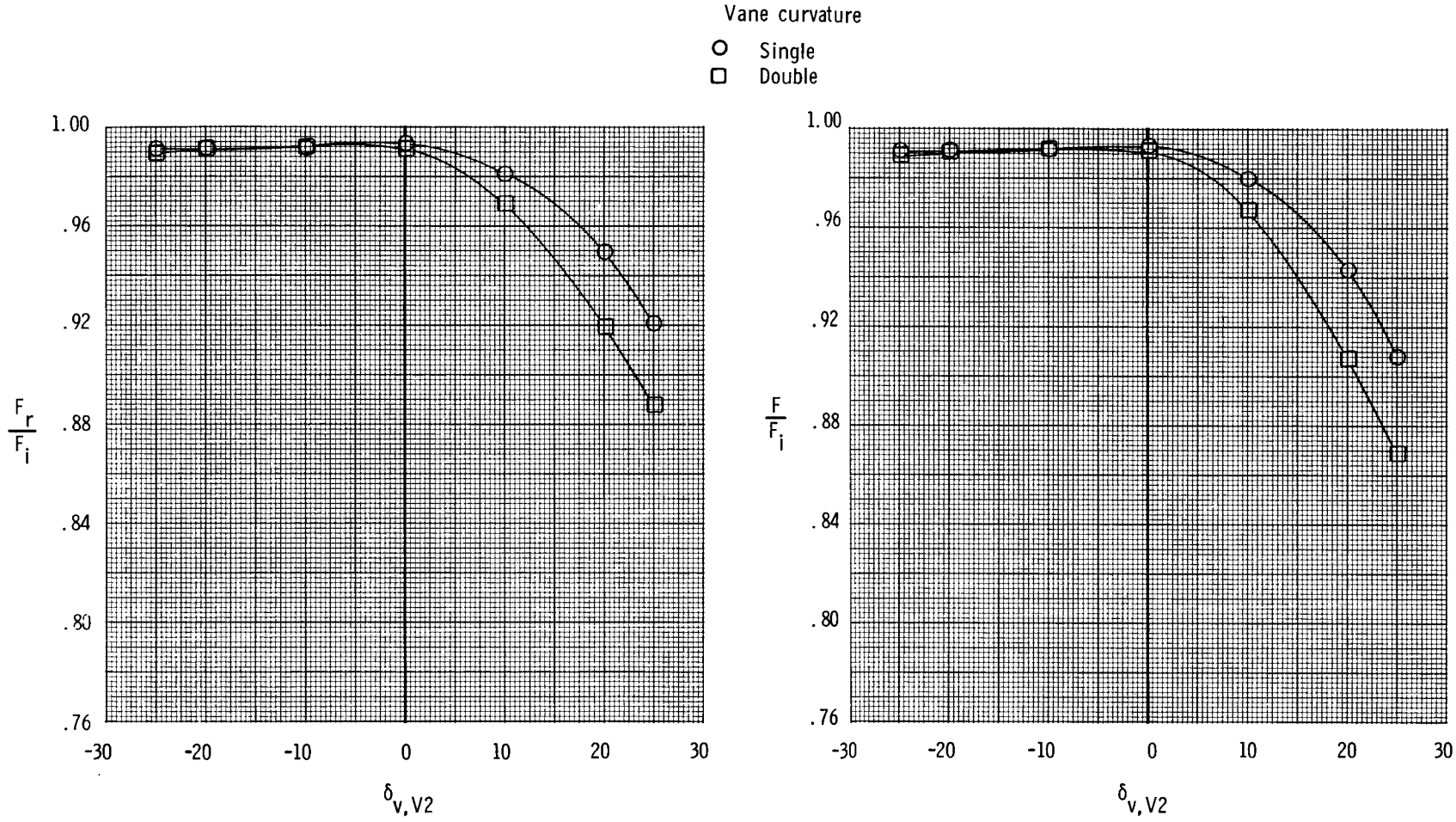

(b) Thrust performance.

Figure 11. Concluded.

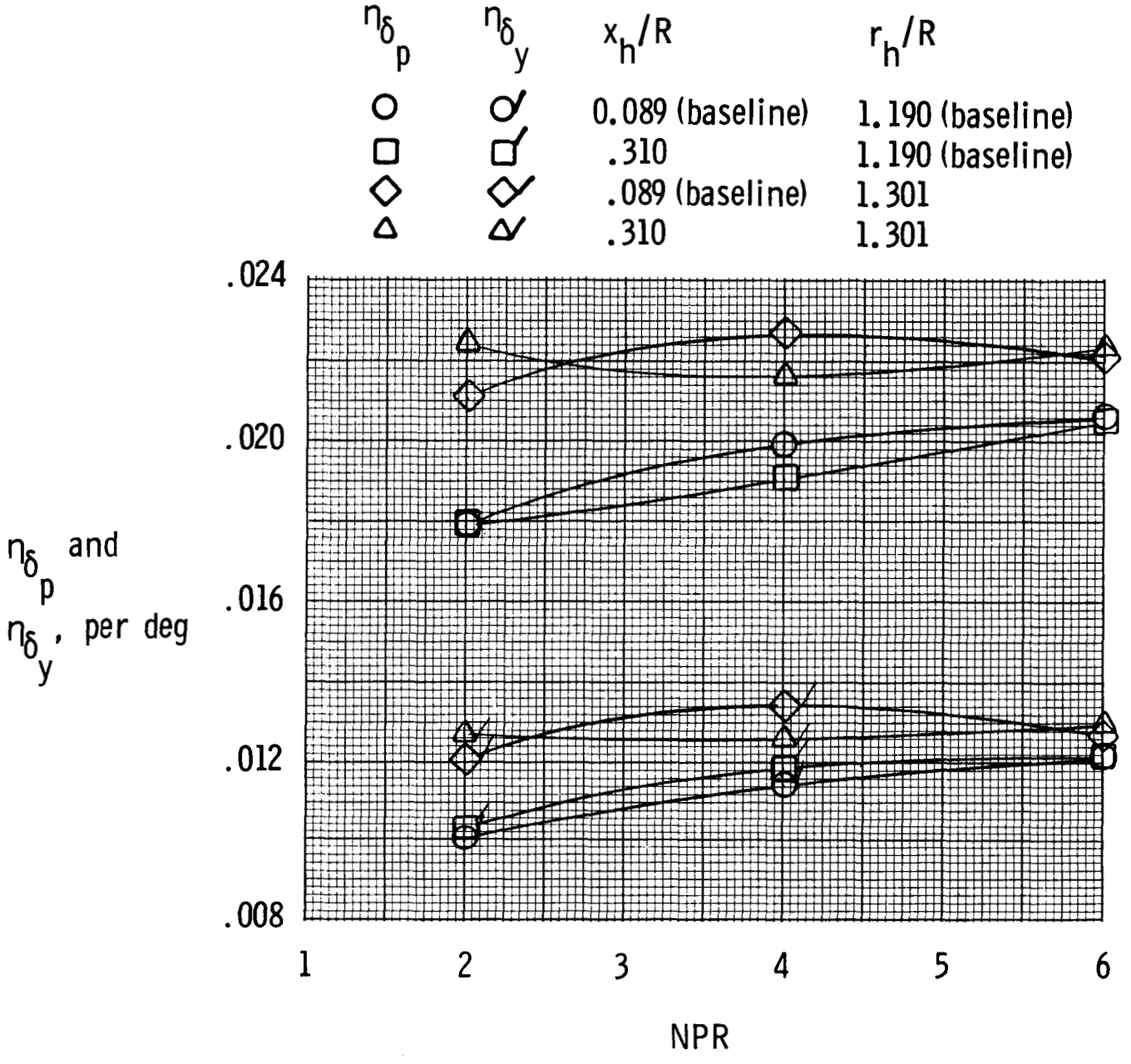

Figure 12. Effect of vane hinge location on body-axis-thrust efficiency with thrust vectoring. Three-vane configurations; $\delta_{v,V1} = \delta_{v,V3} =$ Off; $\delta_{v,V2} = 25°$; double-curvature vanes.

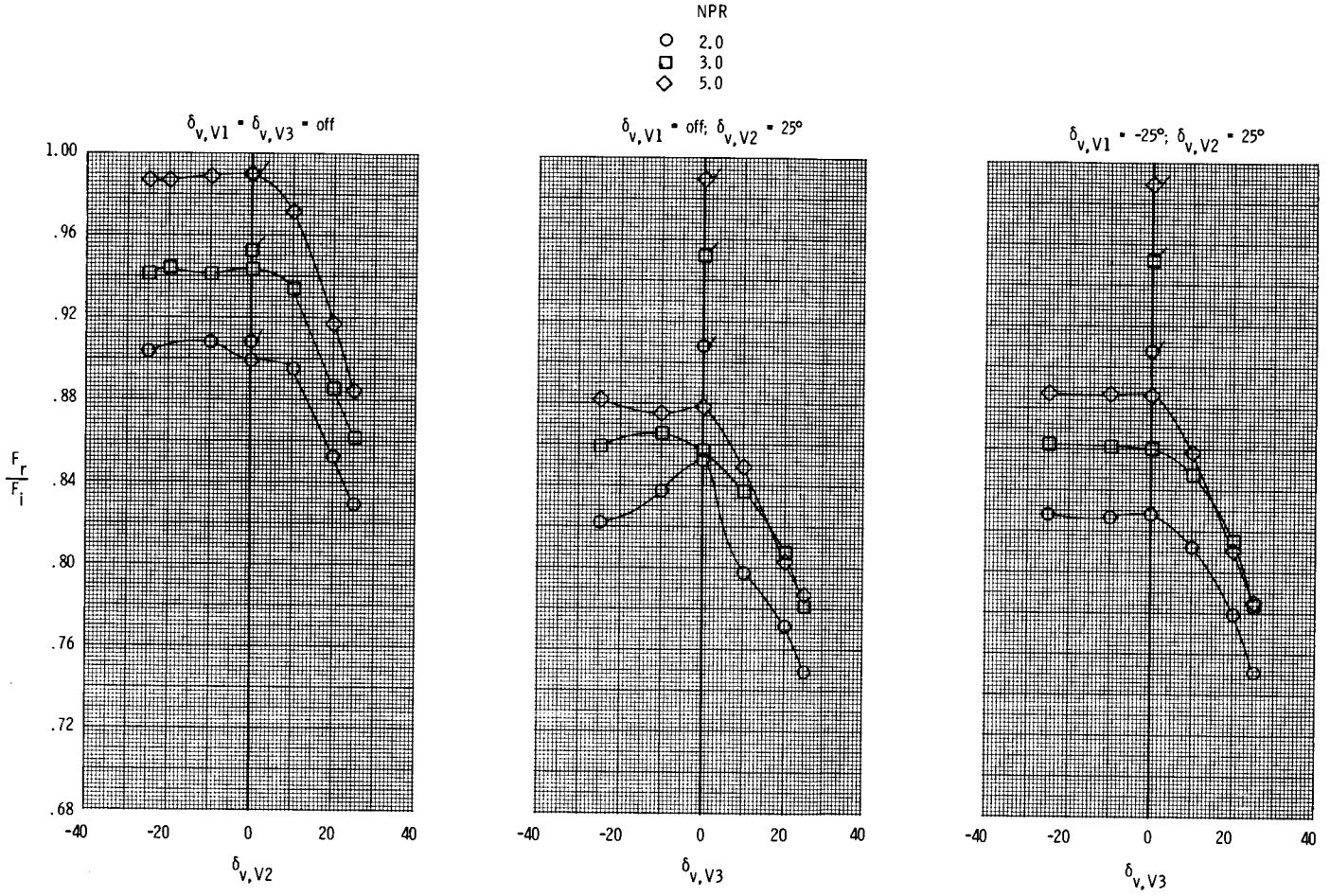

(a) Resultant thrust-ratio performance.

Figure 13. Effect of vane deflection on performance of an axisymmetric C-D nozzle with three vanes for thrust vectoring. Double-curvature vanes; flagged symbols indicate baseline (vanes off) nozzle performance.

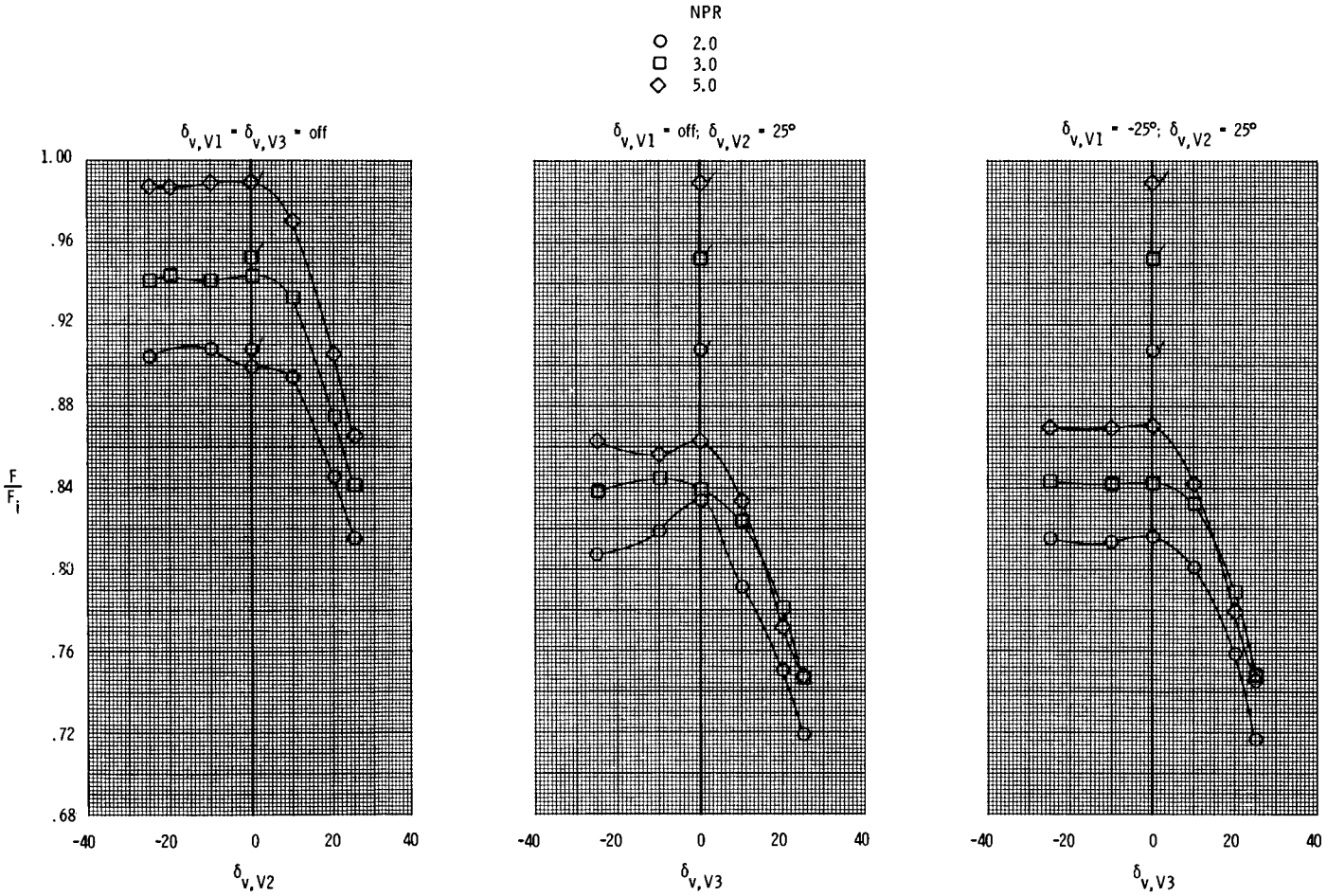

(b) Axial thrust-ratio performance.

Figure 13. Continued.

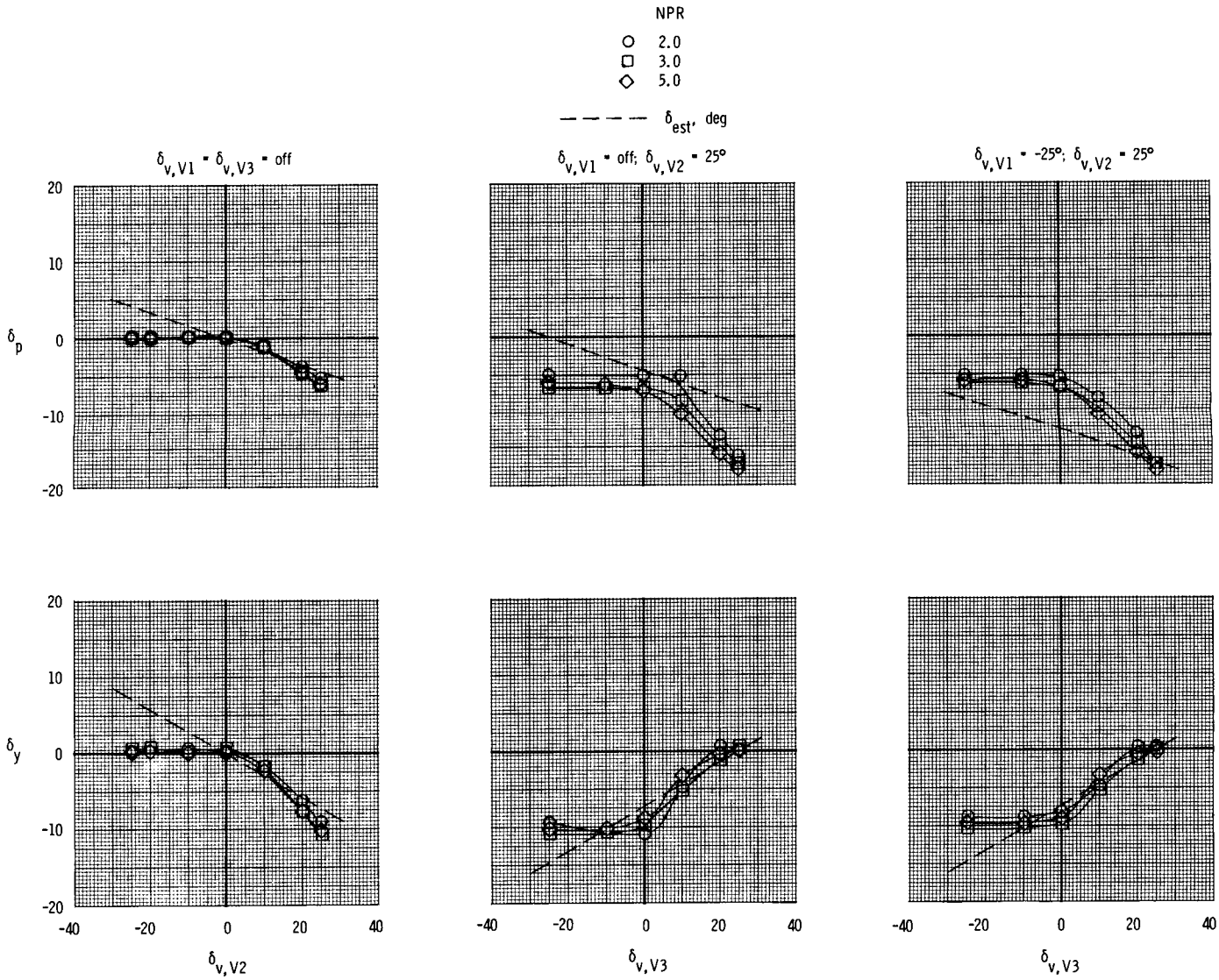

(c) Thrust-vector angle performance.

Figure 13. Concluded.

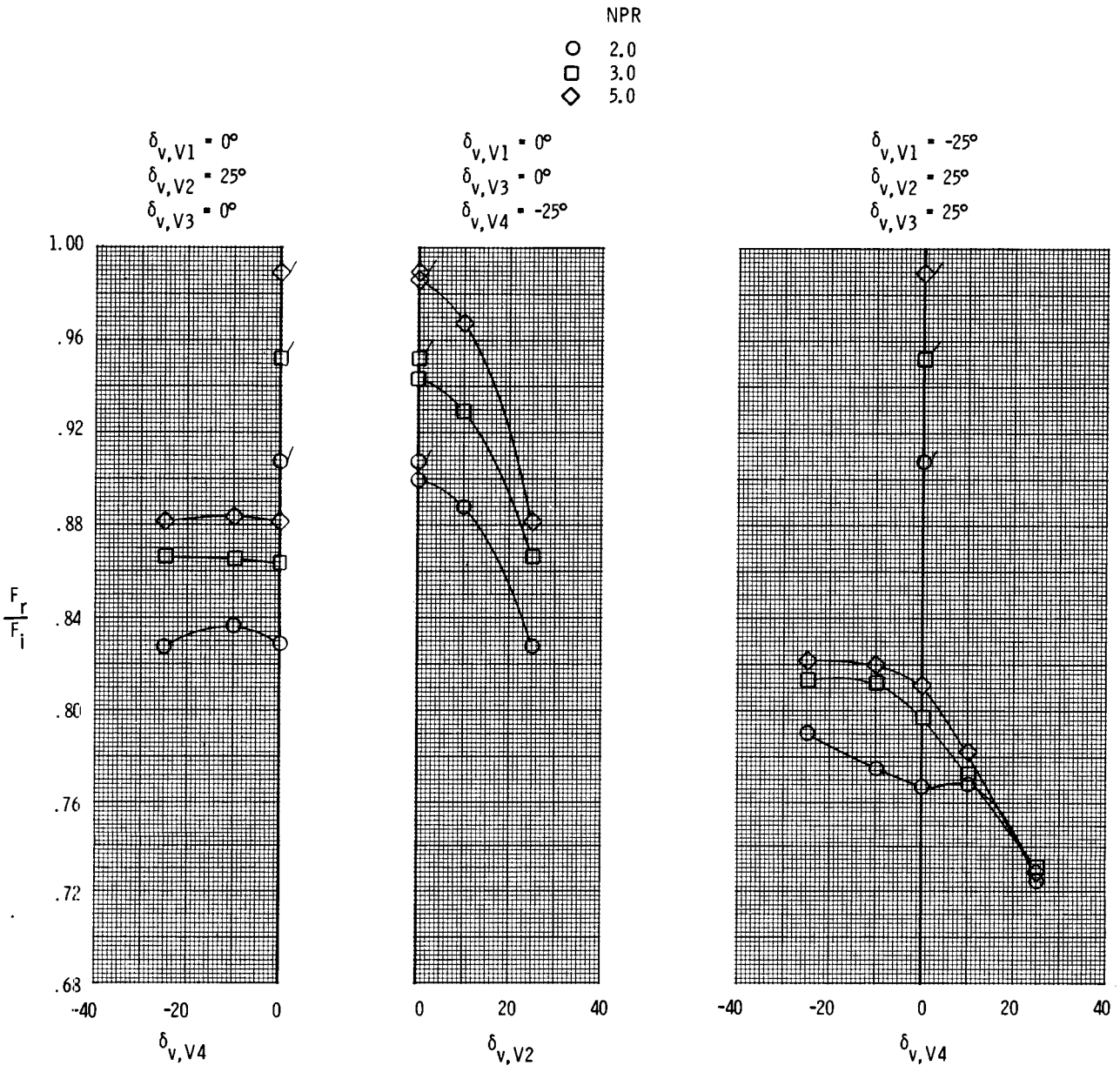

(a) Resultant thrust-ratio performance.

Figure 14. Effect of vane deflection on performance of an axisymmetric C-D nozzle with four vanes for thrust vectoring. Double-curvature vanes; flagged symbols indicate baseline (vanes off) nozzle performance.

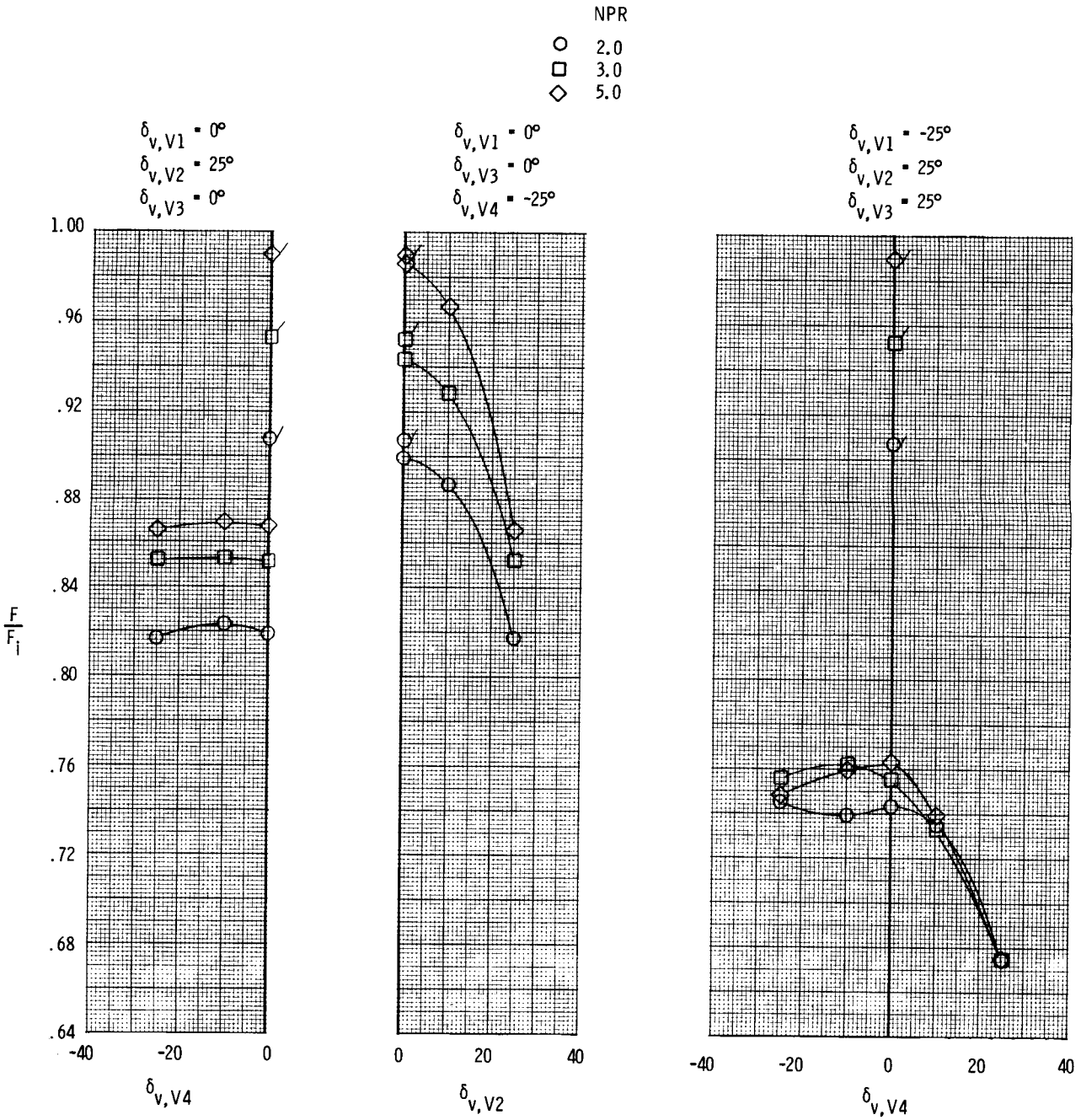

(b) Axial thrust-ratio performance.

Figure 14. Continued.

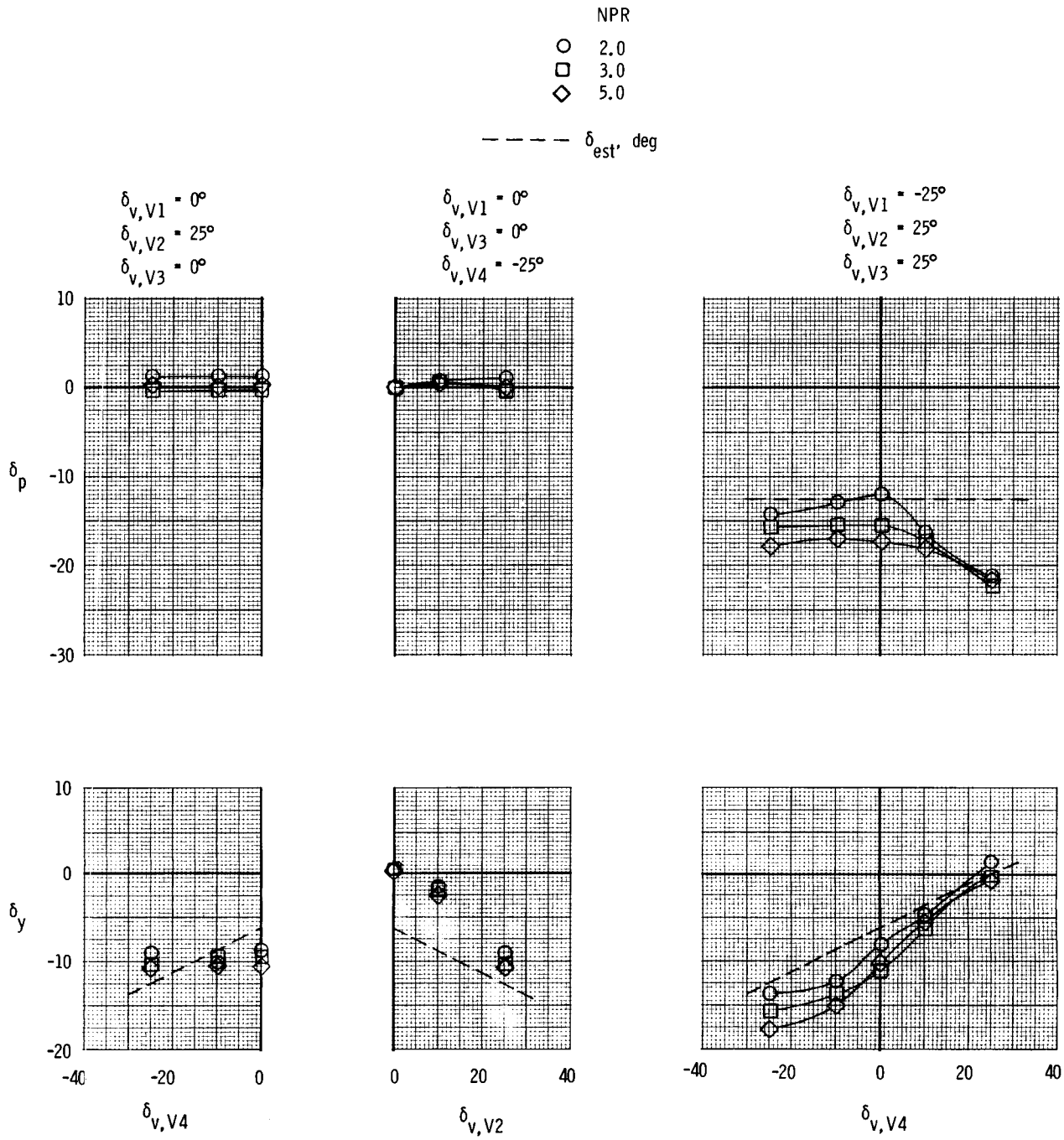

(c) Thrust-vector angle performance.

Figure 14. Concluded.

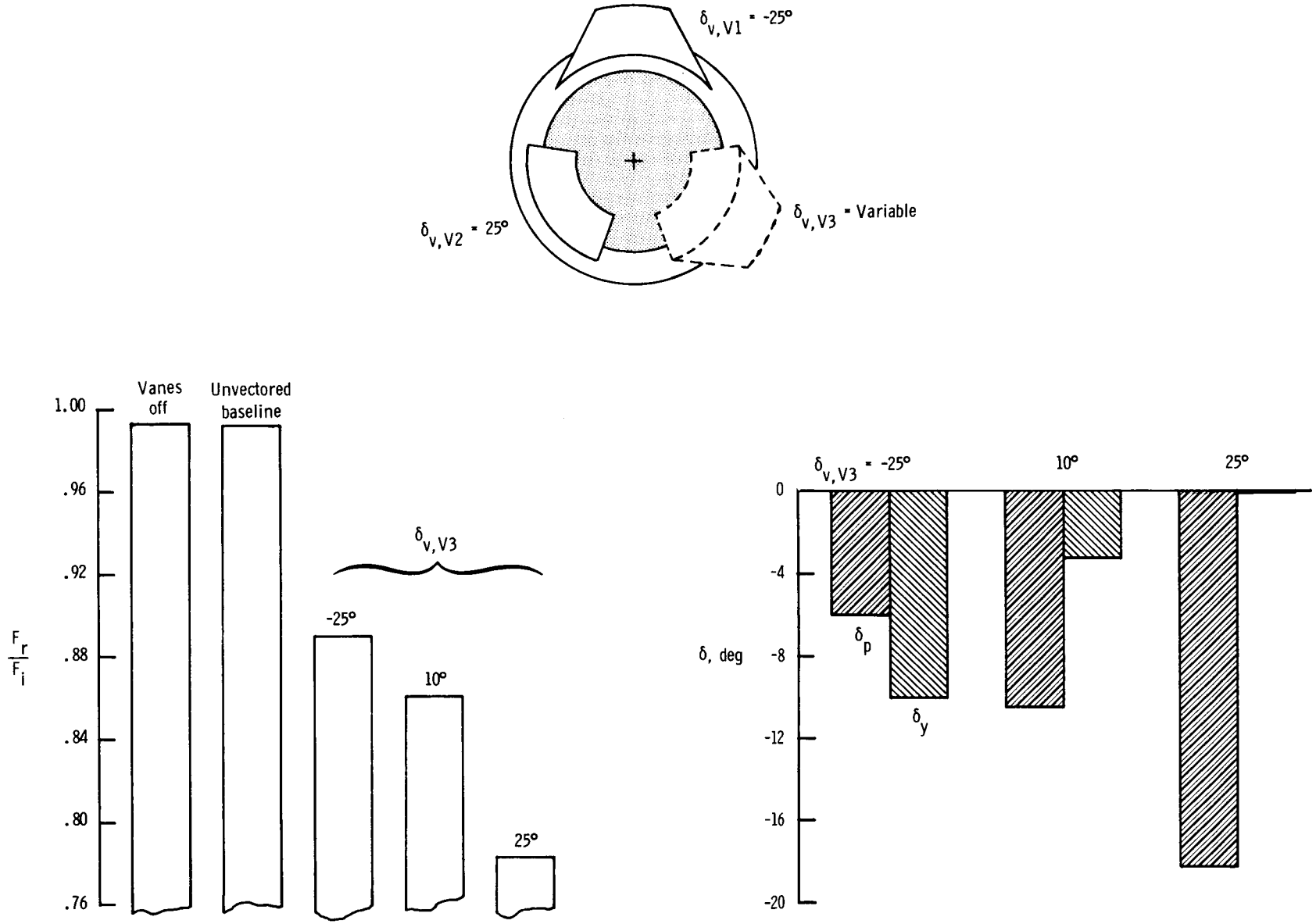

Figure 15. Summary of performance of axisymmetric nozzle with three post-exit vanes. NPR = 6.0.

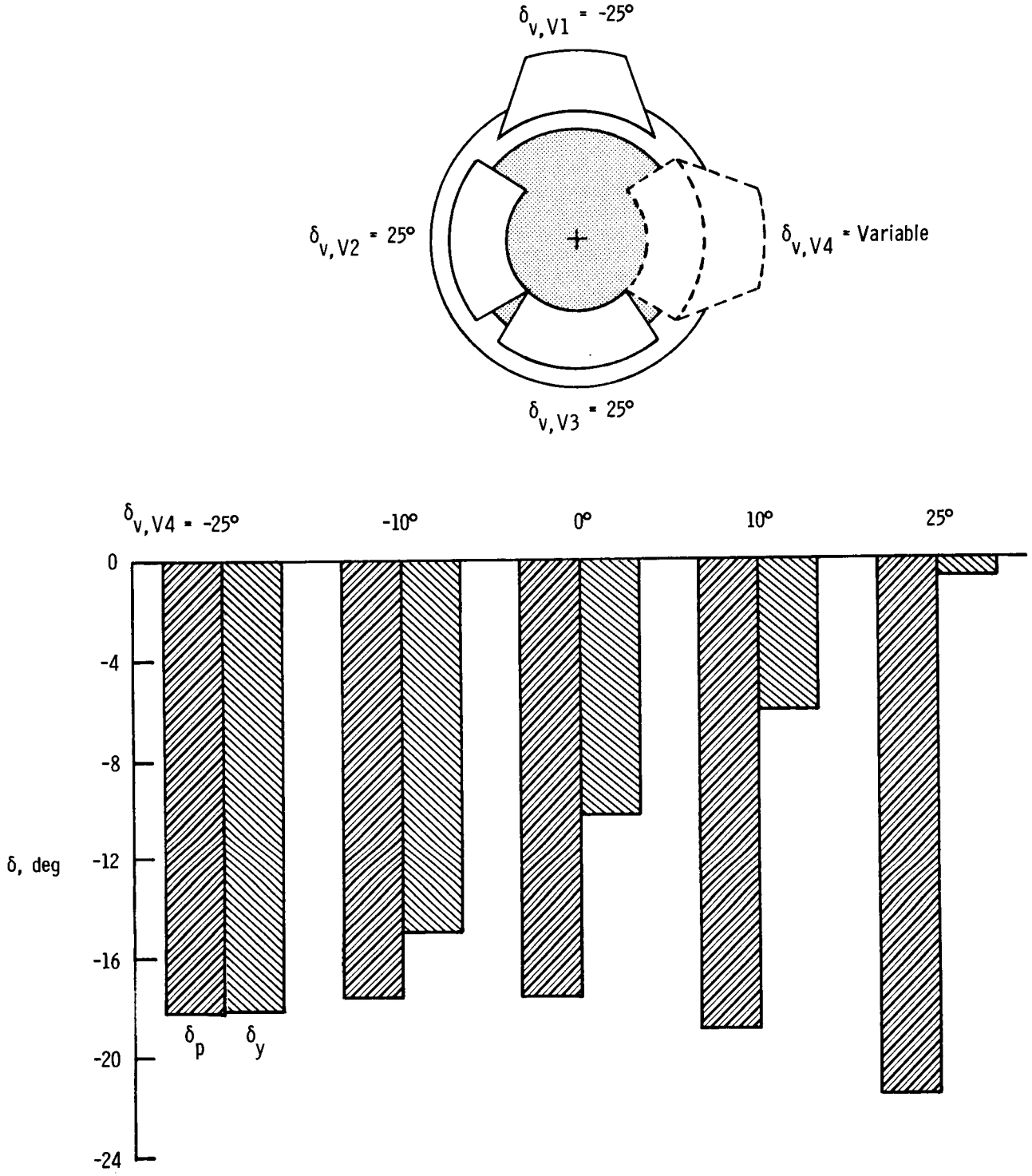

Figure 16. Summary of performance of axisymmetric nozzle with four post-exit vanes. NPR = 6.0.

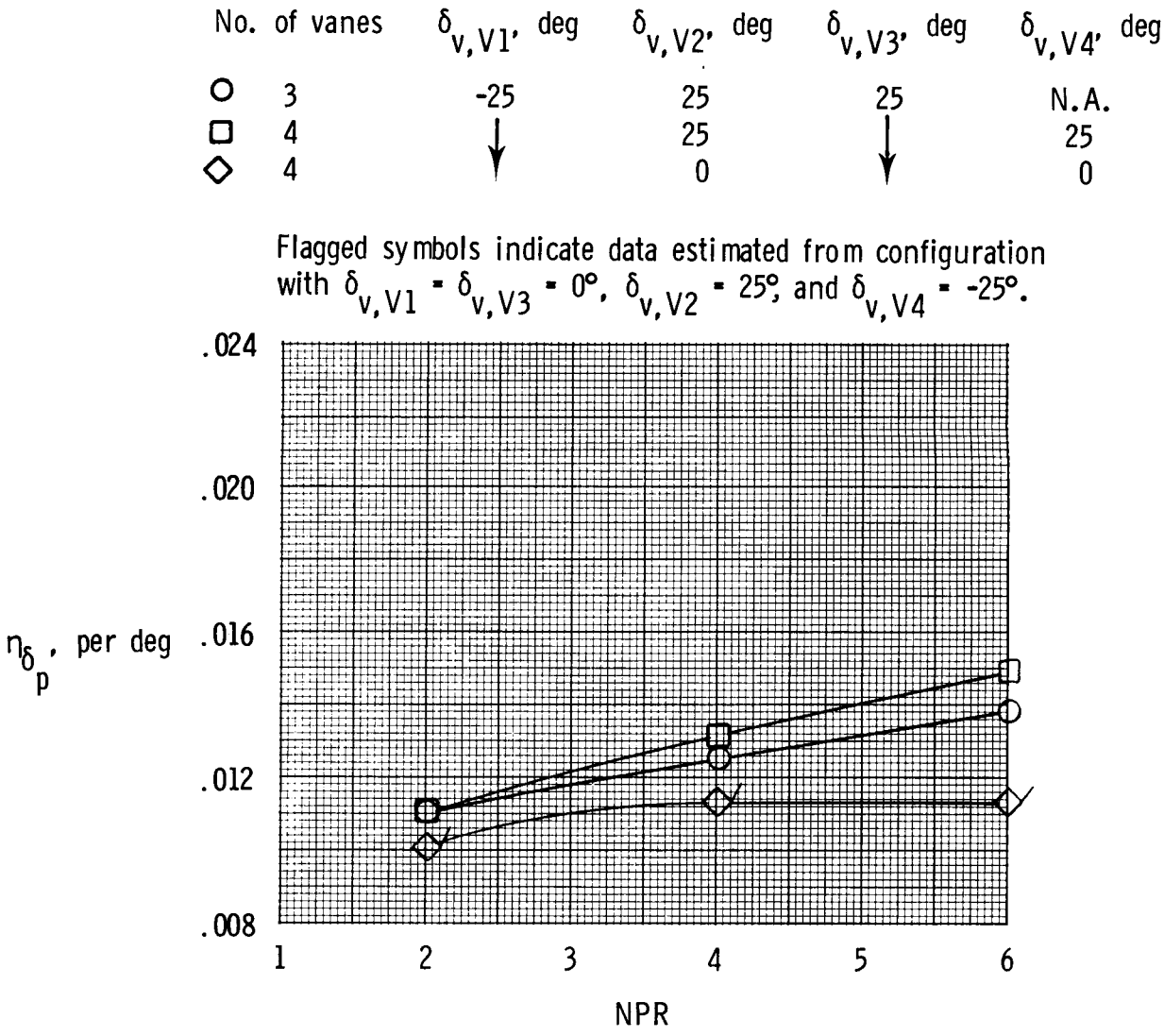

(a) Pitch thrust vectoring.

Figure 17. Effect of number of post-exit vanes on body-axis-thrust efficiency with thrust vectoring. Double-curvature vanes.

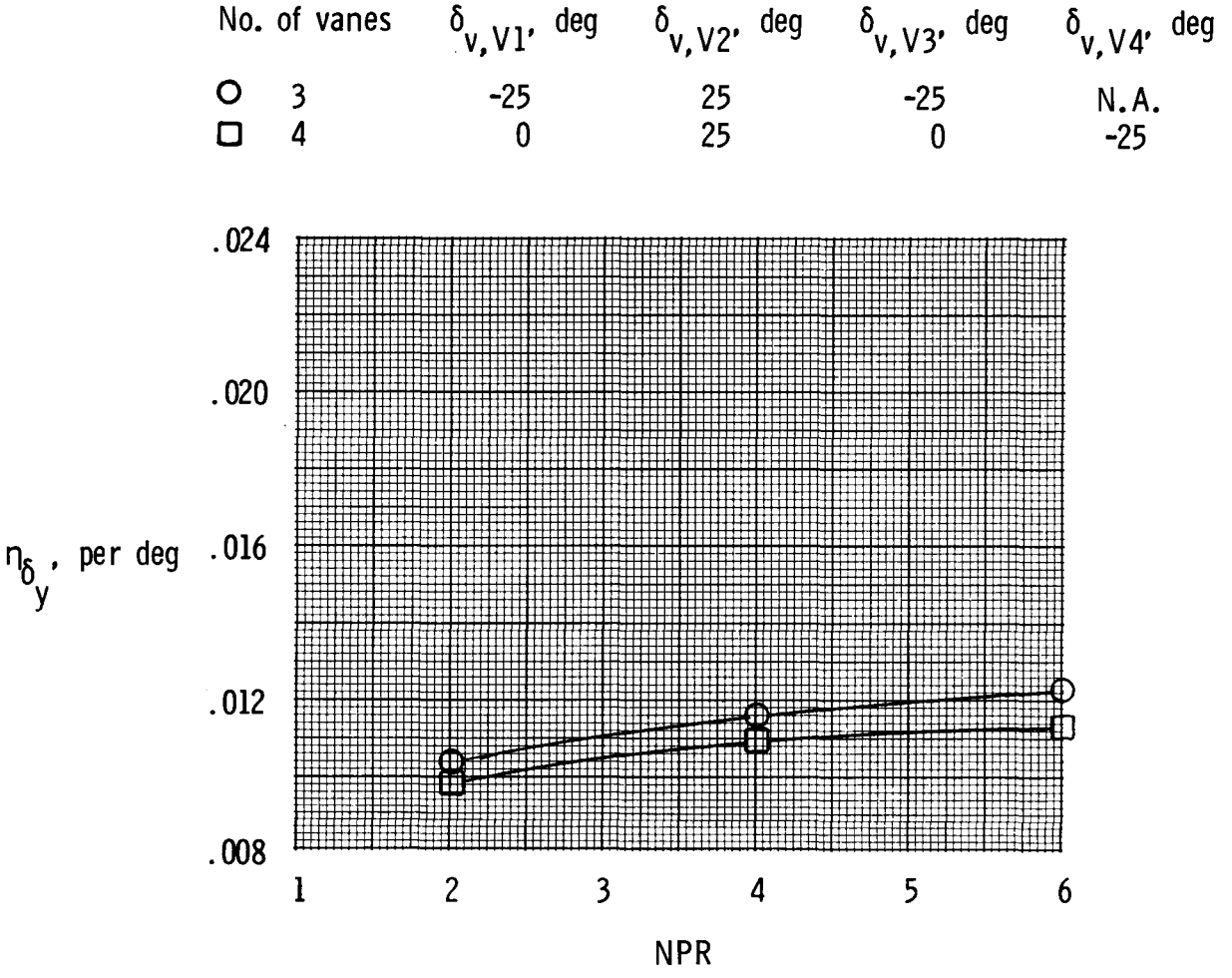

(b) Yaw thrust vectoring.

Figure 17. Continued.

η_{δ_p}	η_{δ_y}	No. of vanes	$\delta_{v,V1}$, deg	$\delta_{v,V2}$, deg	$\delta_{v,V3}$, deg	$\delta_{v,V4}$, deg
○	⟋	3	-25	25	-25	N.A.
□	⟋	4	-25	25	25	-25

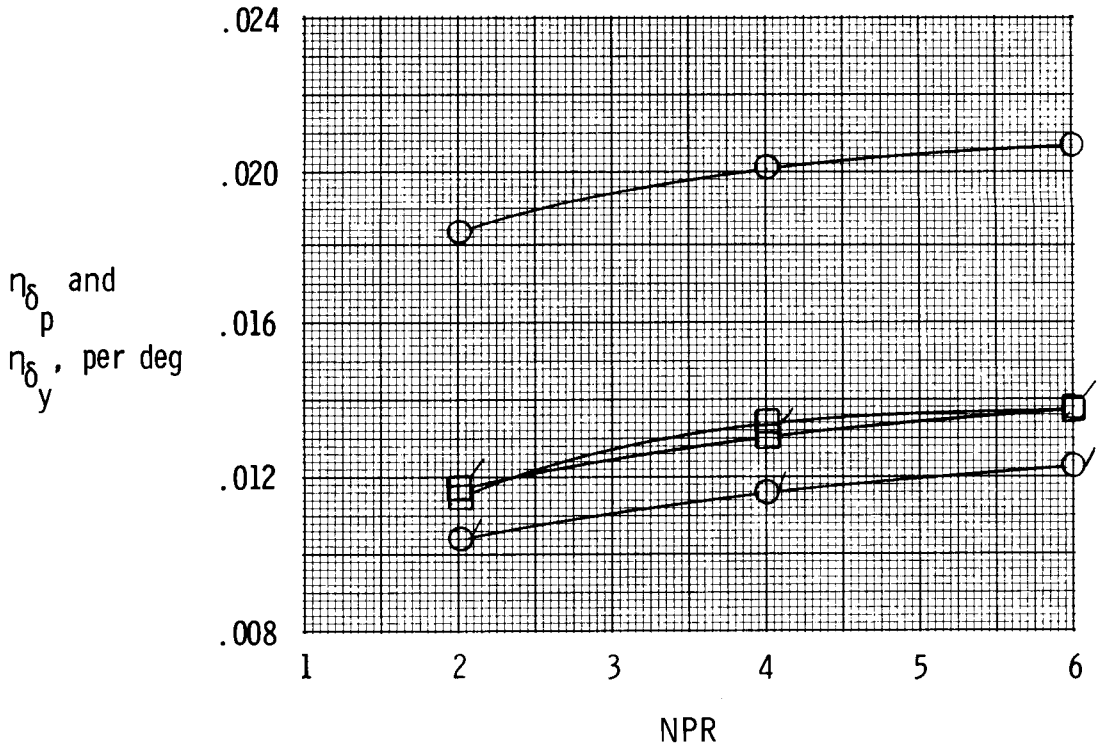

(c) Simultaneous pitch and yaw thrust vectoring.

Figure 17. Concluded.

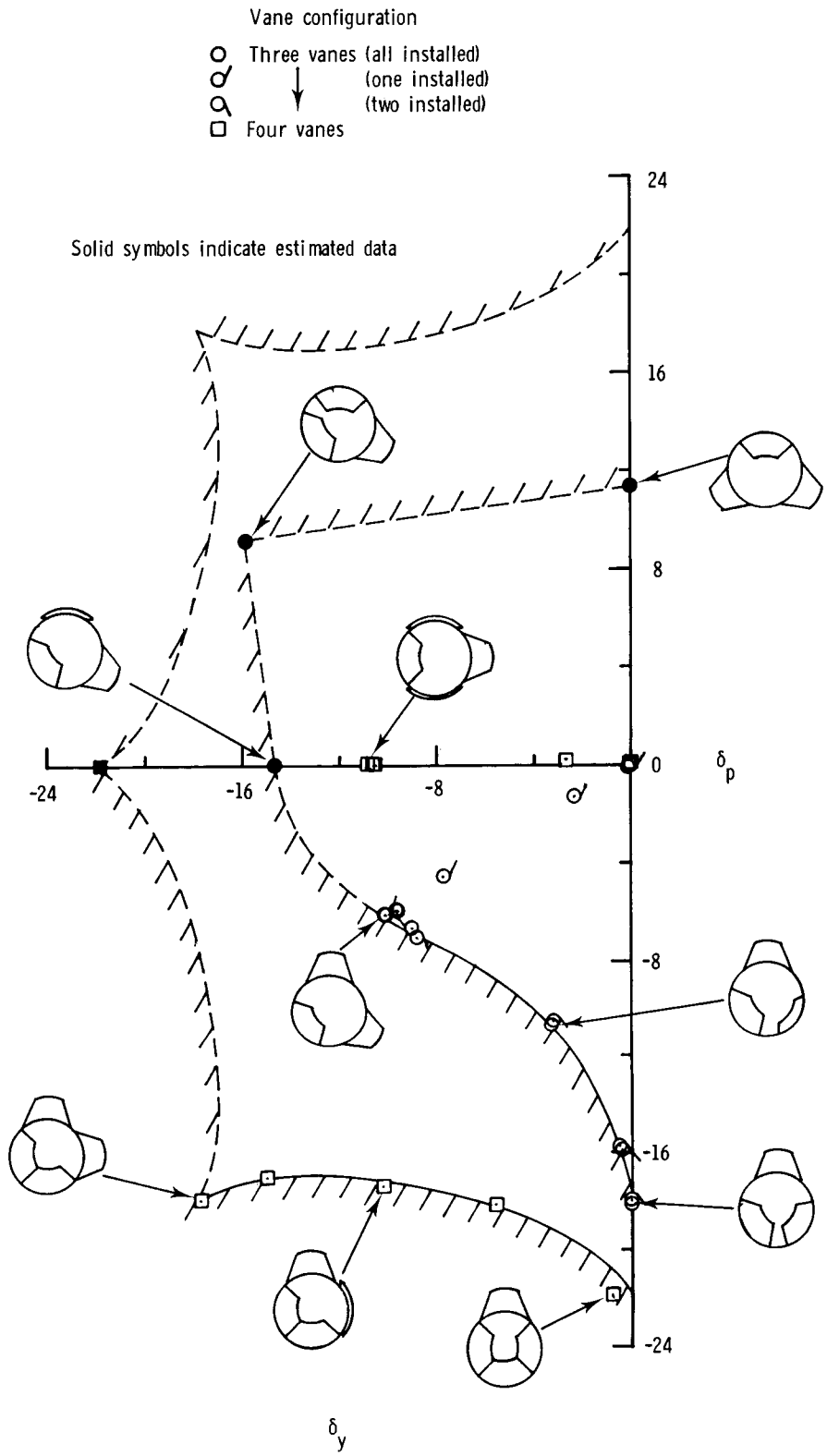

Figure 18. Comparison of resultant yaw and pitch thrust-vector angle envelopes for three-vane and four-vane thrust-vectoring configurations. Double curvature vanes; NPR = 5.0.

	Nozzle	δ_p effector	$\delta_{v,p}$, deg	Reference	Comments
○	Axi.	Three post-exit vanes	-25.0	Current	
○	↓	Three post-exit vanes	25.0	↓	
□		Four post-exit vanes	±25.0		
◇	2-D C-D	Conv. and div. flaps	±11.7	Ref. 32	No yaw vanes
△	2-D C-D	Divergent flaps	±20.3	Ref. 26	Conf. S15; no yaw device
□	SERN	Expansion ramp flap	20.3	Ref. 26	Conf. SR11; no yaw vanes
◇	SERN	Expansion ramp and lower flap	-21.0	Unpublished	Expansion ramp on bottom
◇	2-D C-D	Conv. and div. flaps	±15.0	Ref. 27	Conf. 2
△	2-D C-D	Divergent flaps	±20.0	Ref. 27	Conf. 3; Dihedral angle = 0°

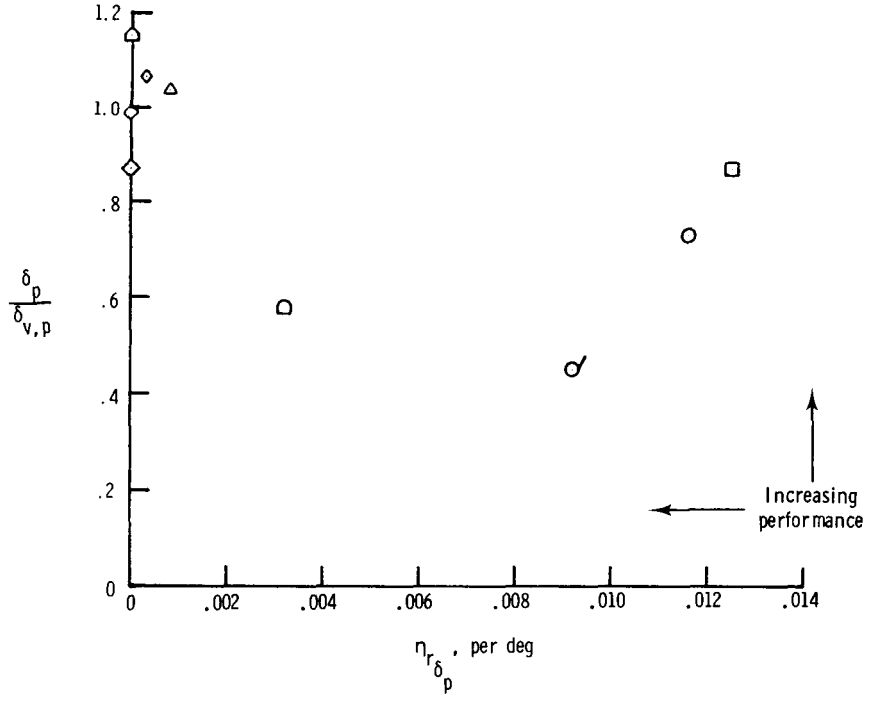

(a) Pitch thrust vectoring, $\delta_{v,y} = 0°$.

Figure 19. Comparison of performance of configurations using different pitch and yaw thrust-vectoring schemes. Data are shown at NPR near design for each configuration.

	Nozzle	δ_y effector	$\delta_{v,y}$, deg	Reference	Comments
□	Axi.	Four post-exit vanes	±25.0	Current	
◇	2-D C-D	Two post-exit vanes	±20.0	Ref. 32	1.5 throat aspect ratio
△	↓	Single flap in one sidewall only	±20.0	Ref. 26	Conf. F16
◁		Round port upstream of throat	±5.3	↓	Conf. P9
◁		Immersed vane (powered rudder)	±20.0		Conf. R4
⌂	SERN	Sidewall vanes at exit	±14.0		Conf. SR5
◇	2-D C-D	Flaps in both sidewalls	±20.0	Ref. 27	Conf. 2
⌂	2-D C-D	Divergent flaps, twin engine	±20.0	Ref. 27	Conf. 3; Dihedral angle = 45°

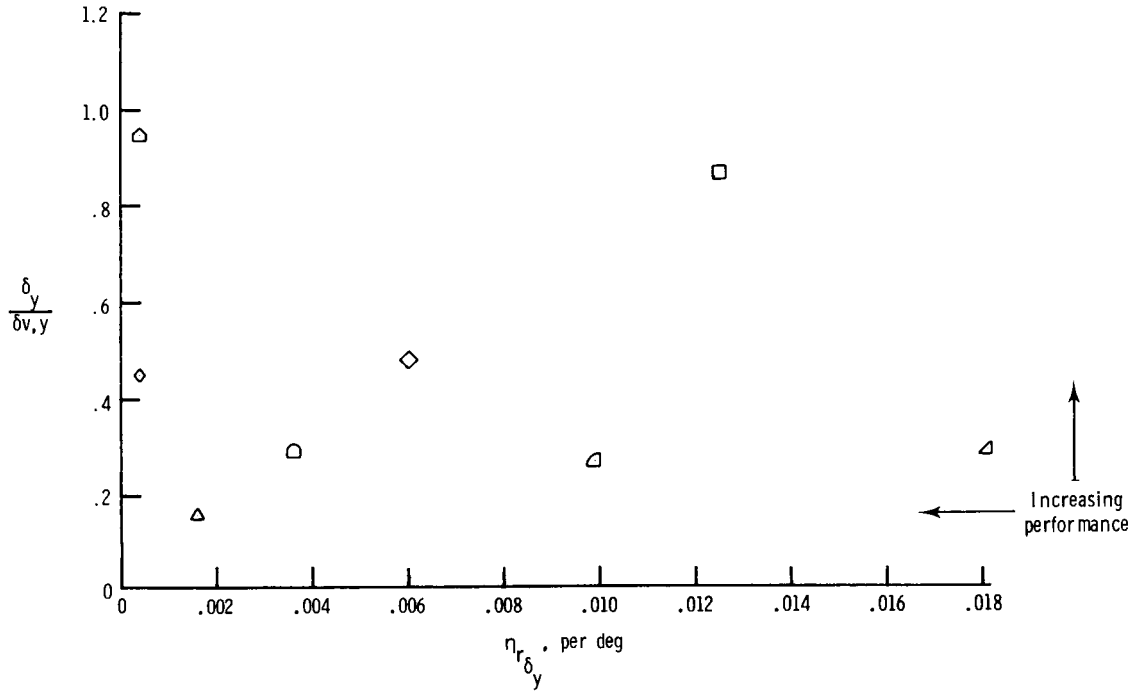

(b) Yaw thrust vectoring, $\delta_{v,p} = 0°$.

Figure 19. Continued.

Nozzle	δ_p effector	$\delta_{v,p}$, deg	δ_y effector	$\delta_{v,y}$, deg	Reference	Comments
Axi.	Three post-exit vanes	-12.5	Three post-exit vanes	±21.7	Current	
↓	Three post-exit vanes	12.5	Three post-exit vanes	±21.7	↓	
↓	Four post-exit vanes	±25.0	Four post-exit vanes	±25.0		
2-D C-D	Conv. and div. flaps	±11.7	Two post-exit vanes	±20.0	Ref. 32	1.5 throat aspect ratio
↓	Divergent flaps	±20.3	Flap in one sidewall only	±20.0	Ref. 26	Conf. F23
↓	↓	↓	Round port upstream of throat	±5.3	↓	Conf. P16
↓	↓	↓	Immersed vane (powered rudder)	±20.0	↓	Conf. R16
SERN	Expansion ramp flap	20.0	Sidewall vanes at exit	±14.0	↓	Conf. SR15
SERN	Expansion ramp and lower flap	-21.0	Tail-pipe gimbal joint	±10.0	Unpublished	Expansion ramp on bottom
2-D C-D	Conv. and div. flaps	±15.0	Flaps in both sidewalls	±20.0	Ref. 27	Conf. 2
2-D C-D	Divergent flaps	±14.1	Divergent flaps	±14.1	Ref. 27	Conf. 3; Dihedral angle = 45°; twin engine; single nozzle deflection of 20°

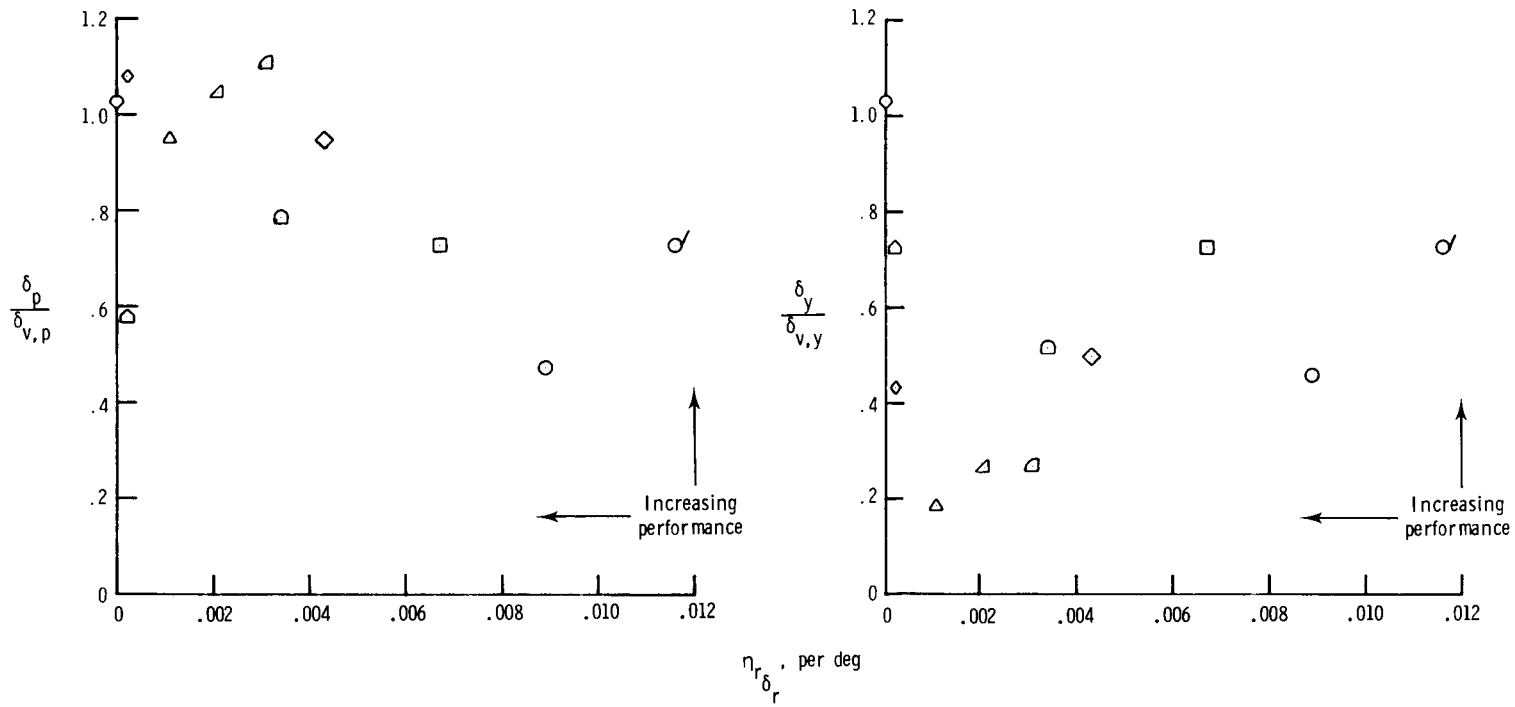

(c) Simultaneous pitch and yaw thrust vectoring.

Figure 19. Concluded.

NASA
National Aeronautics and Space Administration

Report Documentation Page

1. Report No.	2. Government Accession No.	3. Recipient's Catalog No.
NASA TP-2800		

4. Title and Subtitle	5. Report Date
Static Performance of an Axisymmetric Nozzle With Post-Exit Vanes for Multiaxis Thrust Vectoring	May 1988
	6. Performing Organization Code
7. Author(s)	8. Performing Organization Report No.
Bobby L. Berrier and Mary L. Mason	L-16371
	10. Work Unit No.
9. Performing Organization Name and Address	505-68-91-06
NASA Langley Research Center Hampton, VA 23665-5225	11. Contract or Grant No.
12. Sponsoring Agency Name and Address	13. Type of Report and Period Covered
National Aeronautics and Space Administration Washington, DC 20546-0001	Technical Paper
	14. Sponsoring Agency Code

15. Supplementary Notes

16. Abstract

An investigation was conducted in the static test facility of the Langley 16-Foot Transonic Tunnel to determine the flow-turning capability and the nozzle internal performance of an axisymmetric convergent-divergent nozzle with post-exit vanes installed for multiaxis thrust vectoring. The effects of vane curvature, vane location relative to the nozzle exit, number of vanes, and vane deflection angle were determined. A comparison of the post-exit-vane thrust-vectoring concept with other thrust-vectoring concepts is provided. All tests were conducted with no external flow, and nozzle pressure ratio was varied from 1.6 to 6.0.

17. Key Words (Suggested by Authors(s))	18. Distribution Statement
Convergent-divergent nozzle Thrust vectoring Post-exit vanes	Unclassified—Unlimited Subject Category 02

19. Security Classif.(of this report)	20. Security Classif.(of this page)	21. No. of Pages	22. Price
Unclassified	Unclassified	51	A04

For sale by the National Technical Information Service, Springfield, Virginia 22161-2171